Chapter 2
Electromechanical Modeling of Cantilevered Piezoelectric Energy Harvesters for Persistent Base Motions

Alper Erturk and Daniel J. Inman

Abstract This chapter investigates electromechanical modeling of cantilevered piezoelectric energy harvesters excited by persistent base motions. The modeling approaches are divided here into two sections as lumped parameter modeling and distributed parameter modeling. The first section discusses the amplitude-wise correction of the existing lumped parameter piezoelectric energy harvester model for base excitation. For cantilevers operating in the transverse and longitudinal vibration modes, it is shown that the conventional base excitation expression used in the existing lumped parameter models may yield highly inaccurate results in predicting the vibration response of the structure. Dimensionless correction factors are derived to improve the predictions of the coupled lumped parameter piezoelectric energy harvester model. The second section of this chapter presents coupled distributed parameter modeling of unimorph and bimorph cantilevers under persistent base excitations for piezoelectric energy harvesting. Closed-form solutions are obtained by considering all vibration modes and the formal representation of the direct and converse piezoelectric effects. Steady state electrical and mechanical response expressions are derived for arbitrary frequency excitations. These multimode solutions are then reduced to single-mode solutions for excitations around the modal frequencies. Finally, the analytical expressions derived here are validated experimentally for a cantilevered bimorph with a proof mass.

2.1 Introduction

Vibration-based energy harvesting has received a great attention in the past decade. Research motivation in this field is due to the reduced power requirement of small electronic components, such as the wireless sensors used in structural health monitoring applications. The ultimate goal is to power such small electronic devices using the vibration energy available in their ambient so the requirement of an

A. Erturk (✉)

Center for Intelligent Material Systems and Structures, Department of Engineering Science and Mechanics, Virginia Polytechnic Institute and State University, Blacksburg, VA 24061, USA
e-mail: erturk@vt.edu

external power source or periodic battery replacement can be removed or at least minimized. Research in this area involves understanding the mechanics of vibrating structures, the constitutive behavior of piezoelectric materials and the electrical circuit theory. This promising way of powering small electronic components and remote sensors has attracted researchers from different disciplines of engineering, including mechanical, electrical, and civil as well as researchers from the field of material science.

As described by Williams and Yates (1996), the three basic vibration-to-electric energy conversion mechanisms are the electromagnetic (Williams and Yates, 1996, Glynne-Jones et al., 2004, Arnold, 2007), electrostatic (Roundy et al., 2002, Mitcheson, 2004), and piezoelectric (Roundy et al., 2003, Sodano et al., 2005, Jeon et al., 2005) transductions. In the last decade, these transduction mechanisms have been investigated by numerous researchers for vibration-based energy harvesting and extensive discussions can be found in the existing review articles (e.g., Beeby et al., 2006). The literature of the last five years shows that piezoelectric transduction has received the most attention for vibration-to-electricity conversion and four review articles focusing on piezoelectric energy harvesting have been published in the last four years (Sodano et al., 2004a, Priya, 2007, Anton and Sodano, 2007, Cook-Chennault et al., 2008). The relevant experimental research and possible applications of piezoelectric energy harvesting can be found in the aforementioned review articles.

Typically, a piezoelectric energy harvester is a cantilevered beam with one or two piezoceramic layers (a unimorph or a bimorph). The harvester beam is located on a vibrating host structure and the dynamic strain induced in the piezoceramic layer(s) generates an alternating voltage output across the electrodes covering the piezoceramic layer(s). In addition to the experimental research on the practical applications of such energy harvesters, researchers have proposed various mathematical models. Developing a reliable mathematical model can allow predicting the electrical power output of a given energy harvester under the prescribed base excitation conditions. Moreover, it can allow designing and optimizing the energy harvester for a given set of electrical and mechanical variables. Although the implementation of piezoelectric energy harvesting for charging a real battery in an efficient way is more sophisticated (Ottman et al., 2002), researchers have considered a resistive load in the electrical circuit to come up with simple models for predicting the electrical response of the harvester for a given base motion input.

The coupled problem of predicting the voltage across the resistive load connected to the electrodes of a vibrating energy harvester (under base excitation) has been investigated by many authors. In the early mathematical modeling treatments, researchers (Roundy et al., 2003, duToit et al., 2005) employed lumped parameter (single-degree-of-freedom) type solutions. Lumped parameter modeling is a convenient modeling approach since the electrical domain already consists of lumped parameters: a capacitor due to the internal (or inherent) capacitance of the piezoceramic and a resistor due to an external load resistance. Hence, the only thing required is to obtain the lumped parameters representing the mechanical domain so that the mechanical equilibrium and electrical loop equations can be coupled through the

piezoelectric constitutive relations (IEEE, 1987) and a transformer relation can be established. This was the main procedure followed by Roundy et al. (2003) and duToit et al. (2005) in their lumped parameter model derivations. Although lumped parameter modeling gives initial insight into the problem by allowing simple expressions, it is an approximation limited to a single vibration mode and lacks important aspects of the coupled physical system, such as the information of dynamic mode shape and accurate strain distribution as well as their effects on the electrical response.

Since cantilevered energy harvesters are basically excited due to the motion of their base, the well-known lumped parameter harmonic base excitation relation taken from the elementary vibration texts has been used in the energy harvesting literature for both modeling (duToit et al., 2005) and studying the maximum power generation and parameter optimization (Stephen, 2006, Daqaq et al., 2007). It was shown (Erturk and Inman, 2008a) that the conventional form of the lumped parameter harmonic base excitation relation may yield highly inaccurate results both for the transverse and longitudinal vibrations of cantilevered structures depending on the tip (proof) mass to beam/bar mass ratio. The correction is due to the contribution of the distributed mass of the cantilevered structure to the excitation amplitude, which is not modeled in Roundy et al. (2003) and underestimated due to using the lumped parameter base excitation model in duToit et al. (2005). The contribution of the distributed mass to the excitation amplitude is important especially if the harvester does not have a very large proof mass. Correction factors were derived (Erturk and Inman, 2008a) to improve the predictions of the lumped parameter electromechanical relations (duToit et al., 2005) for cantilevered energy harvesters under base excitation. Amplitude-wise correction of the lumped parameter electromechanical relations is summarized in Section 2.2 of this chapter.

As an improved modeling approach, the Rayleigh–Ritz-type discrete formulation originally derived by Hagood et al. (1990) for piezoelectric actuation (based on the generalized Hamilton's principle for electromechanical systems given by Crandall et al. (1968)) was employed by Sodano et al. (2004b) and duToit et al. (2005) for modeling of cantilevered piezoelectric energy harvesters (based on the Euler–Bernoulli beam theory). The Rayleigh–Ritz model gives a discrete model of the distributed parameter system and it is a more accurate approximation when compared with lumped parameter modeling. In order to represent the electrical outputs analytically, Lu et al. (2004) used the vibration mode shapes obtained from the Euler–Bernoulli beam theory and the piezoelectric-constitutive relation (IEEE, 1987) that gives the electric displacement to relate the electrical outputs to the vibration mode shape. Similar models were given by Chen et al. (2006) and Lin et al. (2007) where the electrical response is expressed in terms of the beam vibration response. The deficiencies in these analytical-modeling attempts include lack of consideration of the resonance phenomenon, ignorance of modal expansion, and oversimplified modeling of piezoelectric coupling in the beam equation as viscous damping (e.g., Lu et al., 2004, Chen et al., 2006, Lin et al., 2007). As shown in this work, representing the effect of piezoelectric coupling in the beam equation as viscous damping fails in predicting the coupled system dynamics of a

piezoelectric energy harvester, although this simplified model (viscous damping representation of electromechanical coupling) is a reasonable approximation for certain electromagnetic energy harvesters (Williams and Yates, 1996). One particular consequence of misrepresenting or ignoring piezoelectric coupling in the mechanical equation is highly inaccurate prediction of the optimum load resistance that gives the maximum electrical power (Erturk and Inman, 2008b). Moreover, simplified modeling of piezoelectric coupling cannot predict the variation of the resonance frequencies with changing load resistance. In terms of analytical modeling, Ajitsaria et al. (2007) presented a bimorph cantilever model, where they attempted to combine the static sensing/actuation equations (with constant radius of curvature and a static tip force) with the dynamic Euler–Bernoulli beam equation (where the radius of curvature varies) under base excitation (where there is no tip force). Thus, highly different modeling approaches have appeared in the literature during the last five years and some of them might be misleading due to the simplified modeling approaches presented.

Erturk and Inman (2008c) presented the analytical solution to the coupled problem of a unimorph piezoelectric energy harvester configuration based on the Euler–Bernoulli beam assumptions. They obtained the coupled voltage response across the resistive load and the coupled vibration response of the harvester explicitly for harmonic base excitations in the form of translation with small rotation. The short-circuit and open-circuit trends and the effect of piezoelectric coupling were investigated extensively. Later, Elvin and Elvin (2008) observed the convergence of the Rayleigh–Ritz-type solution formerly introduced by Hagood et al. (1990) to the analytical solution given by Erturk and Inman (2008c) when sufficient number of vibration modes is used with appropriate admissible functions. Erturk and Inman (2008d) extended their closed-form distributed parameter solution to bimorph configurations and presented experimental validations. Section 2.3 of this chapter summarizes the distributed parameter models for the unimorph and bimorph cantilevers and their closed-form solutions (Erturk and Inman, 2008c, 2008d) along with experimental validations. The mathematical derivations, theoretical, and experimental demonstrations presented in Section 2.3 of this chapter aim to provide a basic understanding of piezoelectric energy harvesting and also to clarify the modeling issues observed and repeated in the literature (Erturk and Inman, 2008b).

2.2 Amplitude-Wise Correction of the Lumped Parameter Model

This section discusses the amplitude-wise correction of the coupled lumped parameter piezoelectric energy harvester model for base excitation. The details of the following subsections can be found in Erturk and Inman (2008a). First, the uncoupled lumped parameter base excitation model is reviewed as it is commonly used for representing the mechanical equation of motion in vibration-based energy harvesting. Then the uncoupled distributed parameter solution is presented for cantilevered beams in transverse vibrations and cantilevered bars in longitudinal vibrations and

deficiency of the lumped parameter model is shown. Correction factors are derived for improving the excitation amplitude of the respective lumped parameter models for the transverse and longitudinal vibrations. For the presence of a tip mass (or proof mass), variation of the correction factors tip mass-to-beam/bar mass ratio are presented graphically along with curve-fit relations obtained from numerical solutions. Finally, the amplitude-wise correction factor for longitudinal vibrations is used in the lumped parameter electromechanical equations for improving the coupled lumped parameter predictions.
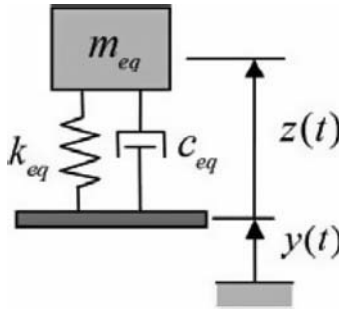
2.2.1 Uncoupled Lumped Parameter Base Excitation Model

Since vibration-based energy harvesters are excited due to the motion of their base, the lumped parameter representation of base excitation model shown in Fig. 2.1 has been used by many authors. The governing equation of motion due to the vibrating base is

$$m_{eq}\ddot{z} + c_{eq}\dot{z} + k_{eq}z = -m_{eq}\ddot{y}, \tag{2.1}$$

where m_{eq}, k_{eq}, and c_{eq} are the equivalent (or effective) mass, stiffness, and viscous damping terms, respectively, y is the base displacement and z is the displacement of the lumped mass relative to the vibrating (or moving) base. Hereafter, an over dot represents differentiation with respect to time and therefore, $\ddot{y}$ is simply the base acceleration. If the base displacement is harmonic in the form of $y(t) = Y_0 \, e^{j\omega t}$ (where Y_0 is the displacement amplitude, ω is the frequency, and j is the unit imaginary number), then the steady-state displacement response of the lumped mass relative to the base becomes

$$z(t) = \frac{\omega^2}{\omega_n^2 - \omega^2 + j2\zeta\omega_n\omega} Y_0 \, e^{j\omega t}, \tag{2.2}$$

Fig. 2.1 Lumped parameter base excitation model

where ω_n is the undamped natural frequency and ζ is the mechanical damping ratio such that $\omega_n = \sqrt{k_{eq}/m_{eq}}$ and $\zeta = c_{eq}/\sqrt{4k_{eq}m_{eq}}$.

In the literature of vibration-based energy harvesting, Eq. (2.1) was first used by Williams and Yates (1996) for modeling the dynamics of their magnet-coil-type electromagnetic generator. The viscous damping coefficient was defined to have an electromagnetically induced component, which allowed expressing the electrical power output of the electromagnetic generator in a convenient way. This simple approach has been employed by several others for modeling of electromagnetic energy harvesters (El-hami et al., 2001, Beeby et al., 2007).

Although modeling of electromechanical coupling in piezoelectric energy harvesting is more complicated than adding an electrically induced viscous damping, the form of Eq. (2.1) was used for the mathematical representation of the piezoelectric energy harvesting problem by Jeon et al. (2005) and Fang et al. (2006) in their experimental papers investigating cantilevered piezoelectric energy harvesters under base excitation. Ajitsaria et al. (2007) used this uncoupled form of lumped parameter base excitation relation for predicting the voltage response of a cantilever, where they did not model piezoelectric coupling in the mechanical equation. As a coupled lumped parameter modeling approach, duToit et al. (2005) introduced piezoelectric coupling to Eq. (2.1) in a formal way (i.e., based on the piezoelectric constitutive laws), rather than introducing an electrically induced viscous damping. However, the origin of their (duToit et al., 2005) mechanical equation was still the conventional lumped parameter base excitation relation given by Eq. (2.1). Since the lumped parameter base excitation model has been widely used in the literature of vibration-based energy harvesting, it is a useful practice to compare its accuracy with the distributed parameter model. The uncoupled distributed parameter solution of the base excitation problem is reviewed in the next section.

2.2.2 Uncoupled Distributed Parameter Base Excitation Model

In the following, the uncoupled distributed parameter solution of the harmonic base excitation problem is reviewed for cantilevered beams in transverse vibrations and for cantilevered bars in longitudinal vibrations.

2.2.2.1 Cantilevered Beams in Transverse Vibrations

Consider the uniform cantilevered beam shown in Fig. 2.2. Based on the Euler–Bernoulli beam assumptions (i.e., shear deformations and rotary inertias are negligible), free vibrations of the beam are governed by the following partial differential equation:

$$YI\frac{\partial^4 w(x,t)}{\partial x^4} + c_s I\frac{\partial^5 w(x,t)}{\partial x^4 \partial t} + c_a\frac{\partial w(x,t)}{\partial t} + m\frac{\partial^2 w(x,t)}{\partial t^2} = 0, \qquad (2.3)$$

where YI is the bending stiffness, m is the mass per unit length, c_a is the external viscous damping term (due to air or the respective surrounding fluid), $c_s I$ is the internal strain rate (or Kelvin–Voigt) damping term, and $w(x, t)$ is the absolute transverse displacement of the beam at point x and time t. Note that both of the damping mechanisms considered here are assumed to satisfy the proportional damping criterion and they are mathematically convenient for the modal analysis solution procedure (Clough and Penzien, 1975, Banks and Inman, 1991). Strain-rate damping is assumed to be stiffness proportional, whereas air damping is assumed to be mass proportional and this type of combined proportional damping is also known as Rayleigh damping (Clough and Penzien, 1975).

As proposed by Timoshenko et al. (1974), the absolute displacement response $w(x, t)$ can be given in terms of the base displacement $w_b(t)$ and the transverse displacement response $w_{rel}(x, t)$ relative to the base as

$$w(x, t) = w_b(t) + w_{rel}(x, t), \tag{2.4}$$

which can be substituted into Eq. (2.3) to yield the following forced vibration equation for the transverse vibrations of the beam relative to its moving base:

$$YI \frac{\partial^4 w_{rel}(x, t)}{\partial x^4} + c_s I \frac{\partial^5 w_{rel}(x, t)}{\partial x^4 \partial t} + c_a \frac{\partial w_{rel}(x, t)}{\partial t} + m \frac{\partial^2 w_{rel}(x, t)}{\partial t^2}$$
$$= -m \frac{d^2 w_b(t)}{dt^2} - c_a \frac{d w_b(t)}{dt}. \tag{2.5}$$

A more general form of the base excitation (with small rotation) is given in the relevant work (Erturk and Inman, 2008a). It is important to note from Eq. (2.5) that the right-hand side forcing function has two components. One component is expectedly due to the distributed inertia of the beam, whereas the other component is due to external viscous damping. The excitation component induced by the external damping component is peculiar to support motion problems. If the surrounding fluid is air, then the excitation term due to air damping is typically negligible when compared with the inertial excitation term. In the absence of a tip mass, it was shown (Erturk and Inman, 2008a) in a dimensionless basis that the contribution from air damping to the excitation force at resonance is less than 5% of the total (inertial and damping) excitation, if the damping ratio due to air damping (defined as ζ_r^a in the following) is less than 2.5%. However, one should be careful with this external damping related excitation term for energy harvesters excited by base motions in fluids with larger damping effect.

Based on the expansion theorem, $w_{rel}(x, t)$ can be represented by an absolutely and uniformly convergent series of the eigenfunctions as

$$w_{rel}(x, t) = \sum_{r=1}^{\infty} \phi_r(x) \eta_r(t), \tag{2.6}$$

Fig. 2.2 Cantilevered beam excited by the motion of its base in the transverse direction

where $\phi_r(x)$ and $\eta_r(t)$ are the mass normalized eigenfunction and the modal response of the clamped-free beam for the rth vibration mode, respectively. In the absence of a tip mass (which is the case in Fig. 2.2), the mass normalized eigenfunctions are

$$\phi_r(x) = \sqrt{\frac{1}{mL}} \left[\cosh \frac{\lambda_r}{L}x - \cos \frac{\lambda_r}{L}x - \sigma_r \left(\sinh \frac{\lambda_r}{L}x - \sin \frac{\lambda_r}{L}x \right) \right], \qquad (2.7)$$

where the λ_r s are the dimensionless frequency numbers obtained from the characteristic equation given by

$$1 + \cos \lambda \cosh \lambda = 0, \qquad (2.8)$$

and σ_r is expressed as

$$\sigma_r = \frac{\sinh \lambda_r - \sin \lambda_r}{\cosh \lambda_r + \cos \lambda_r}. \qquad (2.9)$$

Using Eq. (2.6) in Eq. (2.5) along with the orthogonality conditions of the eigenfunctions (Erturk and Inman, 2008a) yield

$$\ddot{\eta}_r(t) + 2\zeta_r \omega_r \dot{\eta}_r(t) + \omega_r{}^2 \eta_r(t) = [-m\ddot{w}_b(t) - c_a \dot{w}_b(t)] \int_0^L \phi_r(x)\mathrm{d}x, \qquad (2.10)$$

where ω_r is the undamped natural frequency of the rth mode given by

$$\omega_r = \lambda_r{}^2 \sqrt{\frac{YI}{mL^4}}, \qquad (2.11)$$

and ζ_r is the modal mechanical damping ratio and it satisfies the following relation since the strain rate and air damping components are assumed to be stiffness and mass proportional, respectively:

$$\zeta_r = \frac{c_s I \omega_r}{2YI} + \frac{c_a}{2m\omega_r}. \qquad (2.12)$$

If the base displacement is assumed to be harmonic in the form of $w_b(t) = Y_0\, e^{j\omega t}$, the steady-state modal response can be obtained from Eq. (2.10) as

$$\eta_r(t) = \frac{m\omega^2 - j\omega c_a}{\omega_r{}^2 - \omega^2 + j2\zeta_r\omega_r\omega} Y_0\, e^{j\omega t} \int\limits_0^L \phi_r(x)\mathrm{d}x, \qquad (2.13)$$

which can then be used in Eq. (2.6) along with Eq. (2.7) to obtain $w_{\mathrm{rel}}(x, t)$. Then, the transverse displacement at the tip of the beam ($x = L$) relative to the moving base is

$$w_{\mathrm{rel}}(L, t) = Y_0\, e^{j\omega t} \sum_{r=1}^{\infty} \frac{2\sigma_r\, [\cosh\lambda_r - \cos\lambda_r\ -\sigma_r\, (\sinh\lambda_r - \sin\lambda_r)]\, \left(\omega^2 - j2\zeta_r^a\omega_r\omega\right)}{\lambda_r\, \left(\omega_r{}^2 - \omega^2 + j2\zeta_r\omega_r\omega\right)},$$

$$(2.14)$$

where ζ_r^a is the viscous air damping component of the modal mechanical damping ratio ($\zeta_r^a = c_a/2m\omega_r$).

Note that the above analysis is given for a uniform cantilevered beam without a tip mass. Presence of a tip mass changes not only the eigenfunctions and the characteristic equation given by Eqs. (2.7) and (2.8), respectively, but also the excitation term since the inertia of the tip mass also contributes to the forcing function in that case (Erturk and Inman, 2008a). The effect of a tip mass on the ultimate results of the analysis given here (which are the correction factors) is addressed in Section 2.2.3.1.

2.2.2.2 Cantilevered Bars in Longitudinal Vibrations

A similar procedure is applied in this section to obtain the distributed parameter solution of the base excitation problem for the longitudinal vibrations of the uniform cantilevered bar shown in Fig. 2.3. The partial differential equation of motion for free vibrations of the bar can be given by

$$YA\frac{\partial^2 u(x, t)}{\partial x^2} + c_s A\frac{\partial^3 u(x, t)}{\partial x^2 \partial t} - c_a\frac{\partial u(x, t)}{\partial t} - m\frac{\partial^2 u(x, t)}{\partial t^2} = 0, \qquad (2.15)$$
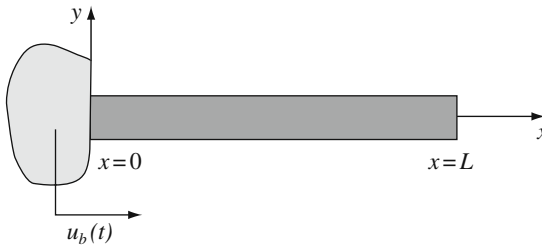
Fig. 2.3 Cantilevered bar excited by the motion of its base in the longitudinal direction

where YA is the axial stiffness, m is the mass per unit length, c_a is the external viscous damping term, $c_s A$ is the internal strain rate damping term, and $u(x, t)$ is the absolute longitudinal displacement of the bar at point x and time t.[1] As in the case of transverse vibrations, strain rate damping is assumed to be stiffness proportional, whereas viscous air damping is assumed to be mass proportional.

The absolute longitudinal displacement response is then represented in terms of the base displacement and the displacement response relative to the base as

$$u(x, t) = u_b(t) + u_{rel}(x, t). \tag{2.16}$$

One can then substitute Eq. (2.16) into Eq. (2.15) to obtain a forced partial differential equation for the longitudinal vibrations of the bar relative to its moving base. After following similar steps given for the transverse vibrations case, the displacement response at the free end of the bar $(x = L)$ relative to its moving base can be expressed for harmonic base displacement $u_b(t) = X_0\, e^{j\omega t}$ as

$$u_{rel}(L, t) = X_0\, e^{j\omega t} \sum_{r=1}^{\infty} \frac{2 \sin \alpha_r \left(1 - \cos \alpha_r\right) \left(\omega^2 - j2\zeta_r^a \omega_r \omega\right)}{\alpha_r \left(\omega_r{}^2 - \omega^2 + j2\zeta_r \omega_r \omega\right)}, \tag{2.17}$$

where X_0 is the harmonic base displacement amplitude (at frequency ω), ω_r is the undamped natural frequency, ζ_r is the modal mechanical damping ratio, ζ_r^a is the viscous air damping component of the modal mechanical damping ratio, and the eigenvalues denoted by α_r are obtained from the following characteristic equation,

$$\cos \alpha_r = 0, \tag{2.18}$$

and the undamped natural frequencies are given by

$$\omega_r = \alpha_r \sqrt{\frac{YA}{mL^2}}. \tag{2.19}$$

Note that the foregoing analysis is valid for a uniform cantilevered bar without a tip mass and details of the derivation in the presence of a tip mass is given by Erturk and Inman (2008a). The effect of a tip mass on the results of the analysis given here is discussed in Section 2.2.3.2.

2.2.3 Correction Factors for the Lumped Parameter Model

In this section, the distributed parameter solutions are reduced to single-mode expressions and these relations are compared with the lumped parameter solution

---

[1] Although the same notation is used for the mass per length and the damping terms in Eqs. (2.3) and (2.15) for convenience, these terms are not necessarily identical.

given by Eq. (2.2). Deficiency of the lumped parameter solution is shown and correction factors are introduced to improve its predictions. For the presence of a tip mass, variation of the correction factors with tip mass-to-beam/bar mass ratio are presented.

2.2.3.1 Cantilevered Beams in Transverse Vibrations

For excitations around the first natural frequency (i.e., for $\omega \cong \omega_1$), the distributed parameter solution given by Eq. (2.14) can be reduced to

$$w_{\text{rel}}(L, t) \cong \frac{\mu_1 \omega^2}{\omega_1{}^2 - \omega^2 + \text{j}2\zeta_1\omega_1\omega} Y_0\, e^{\text{j}\omega t}, \qquad (2.20)$$

which is in the form of the lumped parameter solution given by Eq. (2.2).[2] Thus, μ_1 is the amplitude-wise correction factor for the lumped parameter model (for transverse vibrations) and it can be given by

$$\mu_1 = \frac{2\sigma_1 \left[\cosh \lambda_1 - \cos \lambda_1 \ -\sigma_1 \left(\sinh \lambda_1 - \sin \lambda_1\right)\right]}{\lambda_1}, \qquad (2.21)$$

where subscript 1 stands for the first vibration mode. It is then straightforward to obtain from Eqs. (2.8), (2.9) and (2.21) that $\mu_1 = 1.566$. Here, in correcting the amplitude-wise prediction of Eq. (2.2), it is assumed that the lumped parameter estimate of the undamped natural frequency (ω_n in Eq. (2.2)) is sufficiently accurate (i.e., $\omega_n \cong \omega_1$ where ω_1 is obtained from Eq. (2.11) for $r = 1$). Typically, the following lumped parameter relation is used to predict the natural frequency of a uniform cantilevered beam in transverse vibrations (Lord Rayleigh, 1894)

$$\omega_n = \sqrt{\frac{k_{\text{eq}}}{m_{\text{eq}}}} = \sqrt{\frac{3YI/L^3}{(33/140)mL + M_t}}, \qquad (2.22)$$

where M_t is the tip mass (if exists) and it is zero in the above discussion. It can be shown that the error due to using Eq. (2.22) in predicting the fundamental natural frequency is about 0.5% in the absence of a tip mass (relative to the Euler–Bernoulli model fundamental natural frequency ω_1). The prediction of Eq. (2.22) is improved in the presence of a tip mass.

In order to compare the lumped parameter and the distributed parameter solutions, the *relative displacement transmissibility FRF* (frequency response function) forms a convenient basis and it is simply $z(t)/y(t)$ for the lumped parameter model and $w_{\text{rel}}(L, t)/w_b(t)$ for the distributed parameter model. Figure 2.4a shows the amplitude-wise error in the lumped parameter displacement transmissibility FRF as a function of dimensionless frequency $\Omega = \omega/\omega_1$ where the correct solution is taken as the distributed parameter solution given by Eq. (2.14). It is clear from

---

[2] Note that the excitation component due to viscous air damping is neglected in Eq. (2.20).
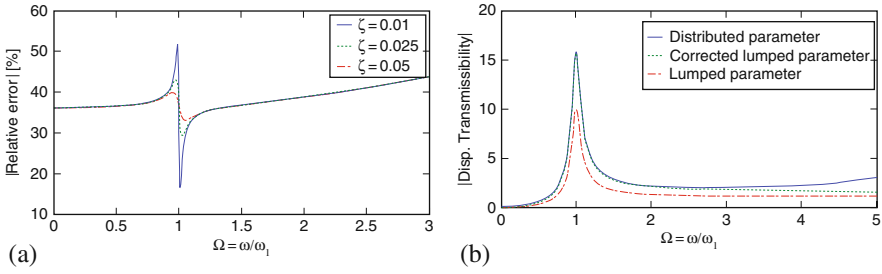
Fig. 2.4 (**a**) Relative error in the lumped parameter displacement transmissibility FRF and the (**b**) displacement transmissibility FRFs obtained from the distributed parameter, corrected lumped parameter, and lumped parameter models

Fig. 2.4a that the error due to using the lumped parameter approach for predicting the relative motion at the tip of the beam is very large. In the vicinity of the first natural frequency (i.e., at $\Omega \cong 1$), the error of the lumped parameter model can be greater than 35% regardless of the damping ratio. The interesting behavior in the relative error plot at resonance is due to the slight inaccuracy of the lumped parameter natural frequency prediction by Eq. (2.22), which was mentioned before. If the lumped parameter natural frequency was taken to be identical to the first natural frequency of the Euler–Bernoulli beam model, one would obtain a smooth behavior in the error. At higher frequencies, the error in the lumped parameter model increases drastically as one approaches to the region of the second vibration mode, which cannot be captured by the lumped parameter model.

Figure 2.4b shows the displacement transmissibility FRFs for the distributed parameter solution given by Eq. (2.14), corrected lumped parameter solution given by Eq. (2.20) and the original lumped parameter solution given by Eq. (2.2). The corrected lumped parameter model obtained by Eq. (2.20) or by multiplying Eq. (2.2) with the correction factor μ_1 represents the distributed parameter model perfectly in a wide range of frequencies around the fundamental vibration mode. Note that the corrected lumped parameter model deviates from the distributed parameter model at high frequencies, since it does not include the information of the higher vibration modes.

Based on the above discussion, it can be concluded that the correct form of the lumped parameter equation of motion given by Eq. (2.1) is

$$m_{eq}\ddot{z} + c_{eq}\dot{z} + k_{eq}z = -\mu_1 m_{eq}\ddot{y}, \qquad (2.23)$$

Thus, Eq. (2.2) becomes

$$z(t) = \frac{\mu_1\omega^2}{\omega_n^2 - \omega^2 + j2\zeta\omega_n\omega}Y_0\,e^{j\omega t}. \qquad (2.24)$$

Here, μ_1 corrects the excitation amplitude and therefore the response amplitude of the lumped parameter model. Otherwise, in the absence of a tip mass, the original lumped parameter model underestimates the response amplitude with an error of about 35%.

So far, the case without a tip mass has been discussed. In many cases, a tip mass (or proof mass) is attached rigidly at the free end of the cantilever to tune its fundamental natural frequency to a desired value or to increase its flexibility especially in microscale applications. The presence of a tip mass changes the forcing function due to base excitation as well as the eigenfunctions and the eigenvalues. After working out the problem for the presence of a tip mass, one can obtain the variation of the correction factor with tip mass-to-beam mass ratio as shown in Fig. 2.5a for transverse vibrations. As can be seen from this figure, if the tip mass of the cantilevered beam is very large, the correction factor tends to unity (i.e., as $M_t/mL \to \infty$, $\mu_1 \to 1$). Therefore, there is no need to use the correction factor if a large tip mass is attached to the cantilevered beam. This makes perfect physical sense, since the contribution of the distributed mass of the beam to the excitation amplitude becomes negligible in the presence of a large tip mass. In such a case, there is no need to correct the original form of the lumped parameter solution given by Eq. (2.2). The curve shown in Fig. 2.5a is obtained by numerical solution and the following curve fit relation represents it with an error of less than $9 \times 10^{-3}\%$ for all values of M_t/mL:

$$\mu_1 = \frac{(M_t/mL)^2 + 0.603(M_t/mL) + 0.08955}{(M_t/mL)^2 + 0.4637(M_t/mL) + 0.05718}. \tag{2.25}$$

2.2.3.2 Cantilevered Bars in Longitudinal Vibrations

In a similar way, the distributed parameter solution given by Eq. (2.17) can be reduced to the following expression with the assumption of modal excitation around

(a)

(b)
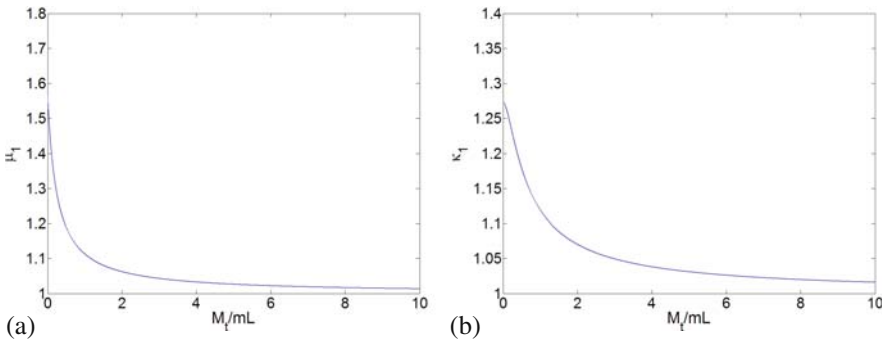
Fig. 2.5 Variation of the correction factor (**a**) with tip mass-to-beam mass ratio for transverse vibrations and (**b**) with tip mass-to-bar mass ratio for longitudinal vibrations

the first natural frequency (i.e., for $\omega \cong \omega_1$):

$$u_{\text{rel}}(L, t) \cong \frac{\kappa_1 \omega^2}{\omega_1{}^2 - \omega^2 + \text{j}2\zeta_1\omega_1\omega} X_0 \, \text{e}^{\text{j}\omega t}, \qquad (2.26)$$

where the excitation due to air damping is neglected. Equation (2.26) is in the form of the lumped parameter solution given by Eq. (2.2) and therefore κ_1 is the amplitude-wise correction factor for the lumped parameter model (for longitudinal vibrations) and it is simply

$$\kappa_1 = \frac{2 \sin \alpha_1 \, (1 - \cos \alpha_1)}{\alpha_1} = \frac{4}{\pi} \cong 1.273, \qquad (2.27)$$

where subscript 1 stands for the first vibration mode. Once again, in correcting the amplitude-wise prediction of Eq. (2.2), it is assumed that the lumped parameter estimate of the undamped natural frequency (ω_n in Eq. (2.2)) is sufficiently accurate (i.e., $\omega_n \cong \omega_1$ where ω_1 is obtained from Eq. (2.19) for $r = 1$). The following lumped parameter relation is commonly used (e.g., duToit et al., 2005) to predict the natural frequency of a uniform cantilevered bar in longitudinal vibrations (Lord Rayleigh, 1894)

$$\omega_n = \sqrt{\frac{k_{\text{eq}}}{m_{\text{eq}}}} = \sqrt{\frac{Y A/L}{m L/3 + M_{\text{t}}}}, \qquad (2.28)$$

where M_{t} is the tip mass (if exists) and it is zero in the above discussion. In the absence of a tip mass, this expression gives an error of about 10.3% (compared with the distributed parameter model fundamental natural frequency ω_1 obtained from Eq. (19)) and the prediction of Eq. (2.28) is improved in the presence of a tip mass. However, it is recommended that one should use Eq. (2.19) with $r = 1$ to predict the fundamental natural frequency for longitudinal vibrations rather than using Rayleigh's relation (Eq. (2.28)) especially if the cantilevered bar does not have a large tip mass. Then, from Eqs. (2.2) and (2.26), it can be shown that the error in the predicted motion transmissibility using the former expression can be as high as 21.4% in the absence of a tip mass even if the accurate natural frequency is used in Eq. (2.2).

As in the case of transverse vibrations, the base excitation problem in the presence of a tip mass can be studied and the variation of the correction factor κ_1 with tip mass-to-bar mass ratio can be obtained as shown in Fig. 2.5b. Equation (2.17) takes a more complicated form in the presence of a tip mass (Erturk and Inman, 2008a). Expectedly, the correction factor tends to unity for large values of tip mass due to the reasoning given in the transverse vibrations case (Section 2.2.3.1). Therefore, there is no need to correct the original lumped parameter model if the cantilevered bar has a sufficiently large tip mass. Otherwise, in order not to underestimate the vibration response of the bar, the lumped parameter relations given by Eqs. (2.1) and (2.2) must be corrected to

$$m_{eq}\ddot{z} + c_{eq}\dot{z} + k_{eq}z = -\kappa_1 m_{eq}\ddot{y}, \tag{2.29}$$

and

$$z(t) = \frac{\kappa_1\omega^2}{\omega_n^2 - \omega^2 + j2\zeta\,\omega_n\omega}Y_0\,e^{j\omega t}, \tag{2.30}$$

respectively. Note that the curve shown in Fig. 2.5b is obtained by numerical solution and the following curve fit relation represents it with an error of less than $4.5 \times 10^{-2}\%$ for all values of M_t/mL:

$$\kappa_1 = \frac{(M_t/mL)^2 + 0.7664(M_t/mL) + 0.2049}{(M_t/mL)^2 + 0.6005(M_t/mL) + 0.161}. \tag{2.31}$$

## 2.2.4 Correction Factor in the Piezoelectrically Coupled Lumped Parameter Equations

We introduce the amplitude-wise correction factor to the piezoelectrically coupled lumped parameter equations. The "general 1D model of piezoelectric vibration energy harvester" shown in Fig. 2.6 as well as the sample numerical values shown in the same figure are from a paper by duToit et al. (2005) and these data are used here for the purpose of demonstration.

The electromechanically coupled equations of the lumped parameter model shown in Fig. 2.6 were given by (duToit et al., 2005).[3]

$$\ddot{u}_{rel}(t) + 2\zeta\omega_n\dot{u}_{rel}(t) + \omega_n^2 u_{rel}(t) - \omega_n^2 d_{33}v(t) = -\ddot{u}_b(t), \tag{2.32}$$

$$R_{eq}C_p\dot{v}(t) + v(t) + m_{eq}R_{eq}d_{33}\omega_n^2\dot{u}_{rel}(t) = 0, \tag{2.33}$$
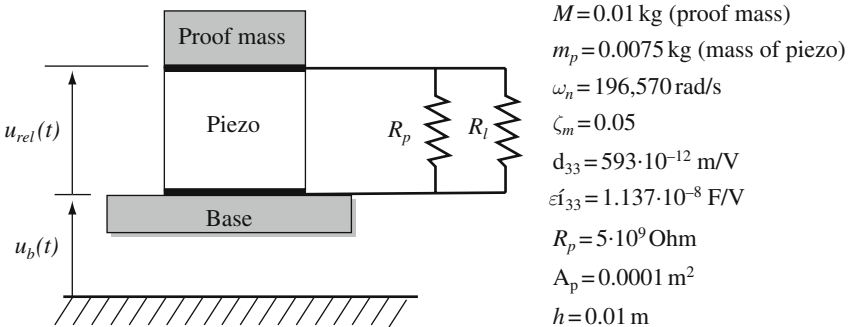
Fig. 2.6 Lumped parameter piezoelectric energy harvester model with sample numerical values by duToit et al. (2005)

---

[3] Some of the variables defined in the relevant work have been adapted to the notation in our text.

where m_{eq} is the equivalent mass of the bar, ζ is the mechanical damping ratio, ω_n is the undamped natural frequency, d_{33} is the piezoelectric constant, R_{eq} is the equivalent resistance (due to the external load resistance R_l and the piezoelectric leakage resistance R_p), C_p is the internal capacitance of the piezoceramic, $u_b(t)$ is the harmonic base displacement, $u_{rel}(t)$ is the displacement of the proof mass relative to the base and $v(t)$ is the voltage output. The lumped parameter model introduced by duToit et al. (2005) is an improved approach with the formal treatment of piezoelectric coupling (which results in the voltage term in the mechanical equation) when compared with the models which considered the effect of piezoelectric coupling as viscous damping. However, based on our previous discussion, we know that the mechanical equilibrium equation given by Eq. (2.32) relies on the lumped parameter base excitation relation given by Eq. (2.1) and it may need a correction factor depending on the proof mass-to-bar mass ratio. From the numerical values given in Fig. 2.6, the proof mass-to-bar mass ratio of this device is $M_t/mL \cong 1.33$. From Fig. 2.5b or Eq. (2.31), the correction factor for the fundamental mode can be obtained as $\kappa_1 \cong 1.0968$. Therefore, the corrected form of Eq. (2.32) is

$$\ddot{u}_{rel}(t) + 2\zeta\omega_n\dot{u}_{rel}(t) + \omega_n^2 u_{rel}(t) - \omega_n^2 d_{33}v(t) = -\kappa_1\ddot{u}_b(t). \qquad (2.34)$$

Note that the resulting vibration amplitude of the proof mass relative to the moving base and the voltage amplitude are linearly proportional to the amplitude of the right-hand side of Eq. (2.34), whereas the power output is proportional to the square of this term:

$$\left|\frac{u_{rel}(t)}{\ddot{u}_b(t)}\right| = \frac{\kappa_1/\omega_n^2\sqrt{1+(r\Omega)^2}}{\sqrt{\left[1-(1+2\zeta r)\Omega^2\right]^2 + \left[\left(1+k_e^2\right)r\Omega + 2\zeta\Omega - r\Omega^3\right]^2}}, \qquad (2.35)$$

$$\left|\frac{v(t)}{\ddot{u}_b(t)}\right| = \frac{\kappa_1 m_{eq} R_{eq} d_{33}\omega_n\Omega}{\sqrt{\left[1-(1+2\zeta r)\Omega^2\right]^2 + \left[\left(1+k_e^2\right)r\Omega + 2\zeta\Omega - r\Omega^3\right]^2}}, \qquad (2.36)$$

$$\left|\frac{P(t)}{\ddot{u}_b^2(t)}\right| = \frac{\kappa_1^2 m_{eq}/\omega_n r k_e^2 R_{eq}/R_l\Omega^2}{\left[1-(1+2\zeta r)\Omega^2\right]^2 + \left[\left(1+k_e^2\right)r\Omega + 2\zeta\Omega - r\Omega^3\right]^2}. \qquad (2.37)$$

Here, $\Omega = \omega/\omega_n$ is the dimensionless frequency (where ω is the excitation frequency), k_e^2 is the coupling coefficient and $r = \omega_n R_{eq} C_p$ (duToit et al., 2005). If the correction factor is not used for the energy harvester device described by the data provided in Fig. 2.6, all of these terms ($u_{rel}(t)$, $v(t)$, and $P(t)$) are underestimated. In such a case, the error in the relative tip motion and the voltage amplitudes is about 8.83%, whereas the error in the electrical power amplitude is about 16.9% (since $\kappa_1 \cong 1.0968$) relative to the distributed parameter solution.

2.3 Coupled Distributed Parameter Models and Closed-Form Solutions

This section presents the distributed parameter models for unimorph and bimorph cantilevers and their closed-form solutions for harmonic base excitation input. The mathematical derivation steps are summarized here and the details of the following subsections can be found in the relevant papers by Erturk and Inman (2008c, 2008d). Experimental validation of the coupled distributed parameter relations is presented for a cantilevered bimorph with a tip mass.

2.3.1 Modeling Assumptions

The three basic cantilevered piezoelectric energy harvester configurations are shown in Fig. 2.7. The first cantilever shown in Fig. 2.7a is a unimorph configuration (with a single piezoceramic layer), whereas the other two cantilevers (Fig 2.7b and c) are bimorph configurations (with two piezoceramic layers). These configurations are modeled here as uniform composite beams for linearly elastic deformations and
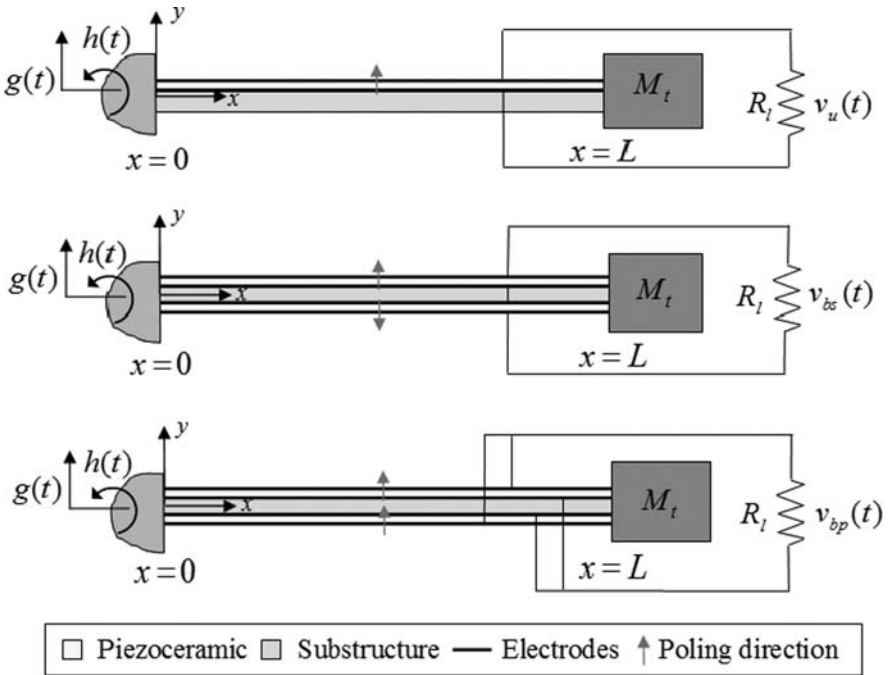
Fig. 2.7 Cantilevered piezoelectric energy harvester configurations under base excitation; (**a**) unimorph configuration, (**b**) bimorph configuration (series connection), and (**c**) bimorph configuration (parallel connection)

geometrically small oscillations based on the Euler–Bernoulli beam assumptions. Therefore, the effects of shear deformation and rotary inertia are neglected and this is a reasonable assumption since typical piezoceramic benders are designed and manufactured as thin beams. The mechanical losses are represented by the internal (strain rate) and external (viscous air) damping mechanisms. The piezoceramic and substructure layers are assumed to be perfectly bonded to each other. The electrodes covering the opposite faces of the piezoceramic layers are assumed to be very thin so that their contribution to the thickness dimension is negligible.

The piezoceramic layers are poled in the thickness direction as depicted in Fig. 2.7. Since the bimorph configurations have two piezoceramic layers, one can connect the electrical outputs of the piezoceramic layers either in series (Fig. 2.7b) or in parallel (Fig. 2.7c). The continuous electrode pairs covering the top and the bottom faces of the piezoceramic layers are assumed to be perfectly conductive so that a single electric potential difference can be defined between them. Therefore, the instantaneous electric fields induced in the piezoceramic layers are assumed to be uniform throughout the length of the beam. A resistive electrical load (R_l) is considered in the circuit along with the internal capacitances of the piezoceramic layers. As mentioned in the introduction, considering a resistive load in the electrical domain is a common practice in modeling of vibration-based energy harvesters. As a consequence, it is assumed that the base motion input is persistent so that continuous electrical outputs can be extracted from the electromechanical system.

2.3.2 Mathematical Background

For each of the configurations shown in Fig. 2.7, free vibrations of the cantilevered beam are governed by

$$\frac{\partial^2 M(x,t)}{\partial x^2} + c_s I \frac{\partial^5 w(x,t)}{\partial x^4 \partial t} + c_a \frac{\partial w(x,t)}{\partial t} + m \frac{\partial^2 w(x,t)}{\partial t^2} = 0, \tag{2.38}$$

which is similar to Eq. (2.3) given in the uncoupled analysis and definition of the relevant terms can be found in Section 2.2.2.1. However, in the coupled treatment given here, the internal bending moment term, $M(x,t)$, which is the first moment of the axial stress integrated over the beam cross-section, yields not only the first term of Eq. (2.3) but also a piezoelectrically induced voltage term. In order to introduce the piezoelectric coupling to the beam equation, the following axial stress expression (IEEE, 1987) must be used in expressing $M(x,t)$ over the thickness of the beam occupied by the piezoceramic layer(s):

$$T_1 = c_{11}^E S_1 - e_{31} E_3. \tag{2.39}$$

Here, T_1 is the axial stress component, S_1 is the axial strain component, c_{11}^E is the elastic stiffness (i.e., Young's modulus) of the piezoceramic layer at constant electric field, e_{31} is the piezoelectric constant, E_3 is the electric field component, and 1- and

3-directions coincide with the longitudinal and thickness directions, respectively (where $c_{11}^E = 1/s_{11}^E$ in terms of the compliance s_{11}^E and $e_{31} = d_{31}/s_{11}^E$ in terms of the piezoelectric constant d_{31} with the plane-stress assumption). Note that the axial strain component at a certain level (y) from the neutral axis of the composite beam is proportional to the curvature of the beam at that position (x):

$$S_1(x, y, t) = -y\frac{\partial^2 w_{\text{rel}}(x, t)}{\partial x^2}. \tag{2.40}$$

The base excitation $w_b(x, t)$ is then introduced to the free vibration equation such that

$$w(x, t) = w_b(x, t) + w_{\text{rel}}(x, t), \tag{2.41}$$

where the base displacement is

$$w_b(x, t) = g(t) + xh(t). \tag{2.42}$$

Here, as depicted in Fig. 2.7, the base excitation consists of translation in the transverse direction (denoted by $g(t)$) and superimposed small rotation (denoted by $h(t)$). Equation (2.41) can then be substituted into Eq. (2.38) to obtain a forced vibration equation for the transverse displacement response of the beam relative to its base ($w_{\text{rel}}(x, t)$):

$$YI\frac{\partial^4 w_{\text{rel}}(x, t)}{\partial x^4} + c_s I\frac{\partial^5 w_{\text{rel}}(x, t)}{\partial x^4 \partial t} + c_a\frac{\partial w_{\text{rel}}(x, t)}{\partial t} + m\frac{\partial^2 w_{\text{rel}}(x, t)}{\partial t^2} + \vartheta v(t)$$
$$\times \left[\frac{d\delta(x)}{dx} - \frac{d\delta(x - L)}{dx}\right] = -[m + M_t\delta(x - L)]\frac{\partial^2 w_b(x, t)}{\partial t^2}, \tag{2.43}$$

where the bending moment term is also expanded (to give a term related to bending stiffness and an electrical term due to piezoelectric coupling) and the excitation force due to air damping is neglected. In Eq. (2.43), $\delta(x)$ is the Dirac delta function, ϑ is the piezoelectric coupling term (given in the following sections), and $v(t)$ is the voltage across the resistive load for the given cantilever configuration (Fig. 2.7). Equation (2.43) is the expanded form of the coupled mechanical equation of motion in the physical coordinates. Note that the electrical and the mechanical terms as well as the piezoelectric coupling term ϑ (Erturk and Inman, 2008c, 2008d) differ for the three configurations shown in Fig. 2.7 as summarized in the following sections. Since a tip mass (M_t) is present in the configurations shown in Fig. 2.7, the right-hand side inertial forcing term of Eq. (2.43) has an additional term compared with Eq. (2.5).

The presence of a tip mass changes the eigenfunctions and the characteristic equation of the free vibration problem. For the modal expansion of the eigenfunctions given by Eq. (2.6), the eigenfunctions to be used in the presence of a tip mass are

$$\phi_r(x) = C_r \left[\cos \frac{\lambda_r}{L}x - \cosh \frac{\lambda_r}{L}x + \varsigma_r \left(\sin \frac{\lambda_r}{L}x - \sinh \frac{\lambda_r}{L}x \right) \right], \qquad (2.44)$$

where ς_r is obtained from

$$\varsigma_r = \frac{\sin \lambda_r - \sinh \lambda_r + \lambda_r (M_t/mL)(\cos \lambda_r - \cosh \lambda_r)}{\cos \lambda_r + \cosh \lambda_r - \lambda_r (M_t/mL)(\sin \lambda_r - \sinh \lambda_r)}, \qquad (2.45)$$

and C_r is a modal constant which should be evaluated by normalizing the eigenfunctions according to the following orthogonality conditions:

$$\int_0^L \phi_s(x)m\phi_r(x)\mathrm{d}x + \phi_s(L)M_t\phi_r(L) + \left[\frac{\mathrm{d}\phi_s(x)}{\mathrm{d}x} I_t \frac{\mathrm{d}\phi_r(x)}{\mathrm{d}x} \right]_{x=L} = \delta_{rs},$$

$$\int_0^L \phi_s(x)YI\frac{\mathrm{d}^4\phi_r(x)}{\mathrm{d}x^4}\mathrm{d}x - \left[\phi_s(x)YI\frac{\mathrm{d}^3\phi_r(x)}{\mathrm{d}x^3} \right]_{x=L} + \left[\frac{\mathrm{d}\phi_s(x)}{\mathrm{d}x}YI\frac{\mathrm{d}^2\phi_r(x)}{\mathrm{d}x^2} \right]_{x=L} = \omega_r^2 \delta_{rs}.$$

$$(2.46)$$

Here, I_t is the rotary inertia of the tip mass M_t and δ_{rs} is Kronecker delta, defined as being equal to unity for $s = r$ and equal to zero for $s \neq r$.

The undamped natural frequencies are obtained using Eq. (2.11); however, in the presence of a tip mass, the eigenvalues of the system are obtained from

$$1 + \cos \lambda \cosh \lambda + \lambda \frac{M_t}{mL}(\cos \lambda \sinh \lambda - \sin \lambda \cosh \lambda) - \frac{\lambda^3 I_t}{mL^3}$$

$$\times (\cosh \lambda \sin \lambda + \sinh \lambda \cos \lambda) + \frac{\lambda^4 M_t I_t}{m^2 L^4}(1 - \cos \lambda \cosh \lambda) = 0. \qquad (2.47)$$

For a single piezoceramic layer operating into a circuit of admittance $1/R_l$ (as in the unimorph configuration, Fig. 2.7a) the coupled electrical circuit equation is obtained from the following relation (IEEE, 1987):

$$\frac{\mathrm{d}}{\mathrm{d}t} \left(\int_A \mathbf{D} \cdot \mathbf{n} \, \mathrm{d}A \right) = \frac{v(t)}{R_l}, \qquad (2.48)$$

where $v(t)$ is the voltage across the electrodes of the piezoceramic, $\mathbf{D}$ is the vector of electric displacement components, $\mathbf{n}$ is the unit outward normal, and the integration is performed over the electrode area A. The relevant component of the electric displacement to be used in the inner product of the integrand of Eq. (2.48) is

$$D_3 = e_{31}S_1 + \varepsilon_{33}^S E_3, \qquad (2.49)$$

where D_3 is the electric displacement component and ε_{33}^S is the permittivity component at constant strain (IEEE, 1987) and $\varepsilon_{33}^S = \varepsilon_{33}^T - d_{31}^2/s_{11}^E$ in terms of the

permittivity at constant stress. Note that the axial strain component S_1 introduces the beam deflection $w_{\mathrm{rel}}(x, t)$ to the circuit equation due to Eq. (2.40), so that Eq. (2.48) yields a coupled electrical circuit equation.

The coupled distributed parameter equations for the cantilevered piezoelectric energy harvester configurations shown in Fig. 2.7 and their closed-form solutions are derived in the following sections based on the foregoing introduction.

2.3.3 Unimorph Configuration

After expressing the coupled beam equation in the physical coordinates (Erturk and Inman, 2008c), the modal expansion and the orthogonality conditions of the vibration modes (given by Eqs. (2.6) and (2.46)) can be used to obtain

$$\ddot{\eta}_r^{\mathrm{u}}(t) + 2\zeta_r\omega_r\dot{\eta}_r^{\mathrm{u}}(t) + \omega_r{}^2\eta_r^{\mathrm{u}}(t) + \chi_r^{\mathrm{u}}v_{\mathrm{u}}(t) = f_r(t), \qquad (2.50)$$

where $\eta_r^{\mathrm{u}}(t)$ is the modal mechanical response of the unimorph cantilever, $v_{\mathrm{u}}(t)$ is the voltage across the resistive load as depicted in Fig. 2.7a, and χ_r^{u} is the *backward* modal coupling term given by

$$\chi_r^{\mathrm{u}} = \vartheta_{\mathrm{u}} \left.\frac{\mathrm{d}\phi_r(x)}{\mathrm{d}x}\right|_L, \qquad (2.51)$$

and

$$\vartheta_{\mathrm{u}} = \frac{e_{31}b}{2h_{\mathrm{pu}}} \left(h_{\mathrm{b}}{}^2 - h_{\mathrm{c}}{}^2\right) \qquad (2.52)$$

is the coupling term in the physical equation, where b is the width of the beam,[4] h_{pu} is the thickness of the piezoceramic layer, and the subscript (or superscript) u stands for the *unimorph* configuration. The positions of the bottom and the top of the piezoceramic layer from the neutral axis are denoted by h_{b} and h_{c}, respectively, and these terms are given in terms of the thicknesses and the Young's moduli ratio of the piezoceramic and the substructure layers in Erturk and Inman (2008c). In Eq. (2.50), the modal mechanical forcing function due to base excitation is

$$f_r(t) = -m \left(\ddot{g}(t) \int_0^L \phi_r(x)\mathrm{d}x + \ddot{h}(t) \int_0^L x\phi_r(x)\mathrm{d}x \right) - M_{\mathrm{t}}\phi_r(L) \left(\ddot{g}(t) + L\ddot{h}(t) \right).$$

$$(2.53)$$

---

[4] The width of the piezoceramic layer(s) (and the electrodes) is assumed to be identical to the width of the substructure layer in the entire analysis.

The electrical circuit equation can be obtained from Eq. (2.48) as

$$\frac{\varepsilon_{33}^{S}bL}{h_{\mathrm{pu}}}\dot{v}_{\mathrm{u}}(t) + \frac{v_{\mathrm{u}}(t)}{R_{l}} = \sum_{r=1}^{\infty}\varphi_{r}^{\mathrm{u}}\dot{\eta}_{r}^{\mathrm{u}}(t),\tag{2.54}$$

where φ_{r}^{u} is the *forward* modal coupling term of the unimorph configuration and can be given by

$$\varphi_{r}^{\mathrm{u}} = -e_{31}h_{\mathrm{pc}}^{\mathrm{u}}b\int_{0}^{L}\frac{\mathrm{d}^{2}\phi_{r}(x)}{\mathrm{d}x^{2}}\mathrm{d}x = -e_{31}h_{\mathrm{pc}}^{\mathrm{u}}b\left.\frac{\mathrm{d}\phi_{r}(x)}{\mathrm{d}x}\right|_{L},\tag{2.55}$$

where $h_{\mathrm{pc}}^{\mathrm{u}}$ is the distance between the neutral axis and the center of the piezoceramic layer.

The forward coupling term φ_{r}^{u} has important consequences as extensively discussed by Erturk et al. (2008c, 2008e). According to Eq. (2.54), which originates from Eq. (2.48), excitation of the simple electrical circuit considered here as well as that of more sophisticated harvesting circuit topologies (Ottman et al., 2002) is proportional to the integral of the dynamic strain distribution over the electrode area. For vibration modes of a cantilevered beam other than the fundamental mode, the dynamic strain distribution over the beam length changes sign at the *strain nodes*. It is known from Eq. (2.40) that the curvature at a point is a direct measure of the bending strain. Hence, for modal excitations, strain nodes are the *inflection points* of the eigenfunctions and the integrand in Eq. (2.55) is the curvature eigenfunction. If the electric charge developed at the opposite sides of a strain node is collected by continuous electrodes for vibrations with a certain mode shape, cancellation occurs due to the phase difference in the mechanical strain distribution. Mathematically, the partial areas under the integrand function of the integral in Eq. (2.55) cancel each other over the domain of integration. As an undesired consequence, the excitation of the electrical circuit, and therefore the electrical outputs may diminish drastically. In order to avoid cancellations, segmented electrodes can be used in harvesting energy from the modes higher than the fundamental mode. The leads of the segmented electrodes can be combined in the circuit in an appropriate manner (Erturk et al., 2008e). Note that the rth vibration mode of a clamped-free beam has $r - 1$ strain nodes, and consequently, the first mode of a cantilevered beam has no cancellation problem. Some boundary conditions are more prone to strong cancellations. For instance, a beam with clamped–clamped boundary conditions has $r + 1$ strain nodes for the rth vibration mode and even the first vibration mode may yield strong cancellations if continuous electrodes are used. This discussion regarding the forward coupling term is valid for the bimorph configurations discussed in the following sections as well as for more sophisticated geometric arrangements. Attention should be given to the mode shape-dependent optimization of the electrode locations to avoid cancellations.

The circuit equation given by Eq. (2.54) is in the form of an RC electrical circuit excited by a current source (all three elements being connected in parallel to each other). Thus, Eq. (2.54) can be rewritten as

$$C_{\text{pu}} \dot{v}_u(t) + \frac{v_u(t)}{R_l} = i_p^u(t), \tag{2.56}$$

where the internal capacitance and the current source terms can be extracted by matching equations (2.54) and (2.56) as

$$C_{\text{pu}} = \frac{\varepsilon_{33}^S b L}{h_{\text{pu}}} \qquad i_p^u(t) = \sum_{r=1}^{\infty} \varphi_r^u \dot{\eta}_r^u(t) \tag{2.57}$$

Equations (2.50) and (2.56) constitute the coupled equations for the modal mechanical response $\eta_r^u(t)$ of the unimorph and the voltage response $v_u(t)$ across the resistive load. If the translational and rotational components of the base displacement given by Eq. (2.42) are harmonic in the forms of $g(t) = Y_0 e^{j\omega t}$ and $h(t) = \theta_0 e^{j\omega t}$, then the modal mechanical forcing function given by Eq. (2.53) can be expressed as $f_r(t) = F_r e^{j\omega t}$, where the amplitude F_r is

$$F_r = \omega^2 \left[m \left(Y_0 \int_0^L \phi_r(x) dx + \theta_0 \int_0^L x \phi_r(x) dx \right) + M_t \phi_r(L) (Y_0 + L\theta_0) \right]. \tag{2.58}$$

Based on the linear electromechanical system assumption, the steady-state modal mechanical response of the beam and the steady-state voltage response across the resistive load are assumed to be harmonic at the same frequency as $\eta_r^u(t) = H_r^u e^{j\omega t}$ and $v_u(t) = V_u e^{j\omega t}$, respectively, where the amplitudes H_r^u and V_u are complex valued. Then, Eqs. (2.50) and (2.56) yield the following two equations for H_r^u and V_u:

$$\left(\omega_r^2 - \omega^2 + j2\zeta_r\omega_r\omega\right) H_r^u + \chi_r^u V_u = F_r, \tag{2.59}$$

$$\left(\frac{1}{R_l} + j\omega C_{\text{pu}}\right) V_u - j\omega \sum_{r=1}^{\infty} \varphi_r^u H_r^u = 0. \tag{2.60}$$

The complex modal mechanical response amplitude H_r^u can be extracted from Eq. (2.59) and can be substituted into Eq. (2.60) to obtain the complex voltage response amplitude V_u explicitly. The resulting complex voltage response amplitude can then be used in $v_u(t) = V_u e^{j\omega t}$ to express the steady-state voltage response as

$$v_u(t) = \frac{\displaystyle\sum_{r=1}^{\infty} \frac{j\omega \varphi_r^u F_r}{\omega_r^2 - \omega^2 + j2\zeta_r\omega_r\omega}}{\dfrac{1}{R_l} + j\omega C_{\text{pu}} + \displaystyle\sum_{r=1}^{\infty} \frac{j\omega \varphi_r^u \chi_r^u}{\omega_r^2 - \omega^2 + j2\zeta_r\omega_r\omega}} e^{j\omega t}. \tag{2.61}$$

The complex voltage amplitude V_u can be substituted into Eq. (2.59) to obtain the steady-state modal mechanical response of the beam as

$$\eta_r^u(t) = \left(F_r - \chi_r^u \frac{\sum_{r=1}^{\infty} \frac{j\omega\varphi_r^u F_r}{\omega_r^2 - \omega^2 + j2\zeta_r\omega_r\omega}}{\frac{1}{R_l} + j\omega C_{pu} + \sum_{r=1}^{\infty} \frac{j\omega\varphi_r^u \chi_r^u}{\omega_r^2 - \omega^2 + j2\zeta_r\omega_r\omega}} \right) \frac{e^{j\omega t}}{\omega_r^2 - \omega^2 + j2\zeta_r\omega_r\omega}.$$

(2.62)

The transverse displacement response of the unimorph relative to the base can be obtained in the physical coordinates by substituting Eq. (2.62) into the modal expansion (Eq. (6)) as

$$w_{rel}^u(x, t) = \sum_{r=1}^{\infty} \left(F_r - \chi_r^u \frac{\sum_{r=1}^{\infty} \frac{j\omega\varphi_r^u F_r}{\omega_r^2 - \omega^2 + j2\zeta_r\omega_r\omega}}{\frac{1}{R_l} + j\omega C_{pu} + \sum_{r=1}^{\infty} \frac{j\omega\varphi_r^u \chi_r^u}{\omega_r^2 - \omega^2 + j2\zeta_r\omega_r\omega}} \right) \frac{\phi_r(x) e^{j\omega t}}{\omega_r^2 - \omega^2 + j2\zeta_r\omega_r\omega}.$$

(2.63)

2.3.4 Bimorph Configurations

As shown in Fig. 2.7, depending on the poling directions of the piezoceramic layers and the connection of the electrode leads, the electrical outputs of the piezoceramic layers can be combined in series or in parallel for bimorph cantilevers. Although the bimorph configurations shown in Fig. 2.7b and 2.7c have the same geometric and material properties, the different combinations of the piezoceramic layers in the electrical circuit (in series or in parallel) changes not only the voltage response across the resistive load, but also the coupled vibration response. The coupled models of these two bimorph configurations are derived in the following.

2.3.4.1 Series Connection of the Piezoceramic Layers

The partial differential equation governing the forced vibrations of the bimorph configuration shown in Fig. 2.7b can be reduced to

$$\ddot{\eta}_r^{bs}(t) + 2\zeta_r\omega_r\dot{\eta}_r^{bs}(t) + \omega_r^2\eta_r^{bs}(t) + \chi_r^{bs}v_{bs}(t) = f_r(t),$$

(2.64)

where $\eta_r^{bs}(t)$ is the modal mechanical response of the bimorph cantilever for series connection of the piezoceramic layers (b stands for *bimorph configuration* and s stands for *series connection*), $v_{bs}(t)$ is the voltage across the resistive load, $f_r(t)$ is the modal mechanical forcing function given by Eq. (2.53), and χ_r^{bs} is the backward modal coupling term given by

$$\chi_r^{bs} = \vartheta_{bs} \frac{d\phi_r(x)}{dx}\bigg|_L,$$

(2.65)

where

$$\vartheta_{\mathrm{bs}} = \frac{e_{31}b}{2h_{\mathrm{pb}}}\left[\frac{h_{\mathrm{sb}}^2}{4} - \left(h_{\mathrm{pb}} + \frac{h_{\mathrm{sb}}}{2}\right)^2\right]$$

(2.66)

is the coupling term in the physical equation. Here, b is the width of the beam, h_{pb} and h_{sb} are the thicknesses of the piezoceramic and the substructure layers of the bimorph configuration shown in Fig. 2.7b, respectively.

The electrical circuit equation for the series connection case is

$$\frac{C_{\mathrm{pb}}}{2}\dot{v}_{\mathrm{bs}}(t) + \frac{v_{\mathrm{bs}}(t)}{R_{\mathrm{l}}} = i_{\mathrm{p}}^{\mathrm{bs}}(t),$$

(2.67)

where the internal capacitance and the current source terms are

$$C_{\mathrm{pb}} = \frac{\varepsilon_{33}^S b L}{h_{\mathrm{pb}}} \qquad i_{\mathrm{p}}^{\mathrm{bs}}(t) = \sum_{r=1}^{\infty}\varphi_r^{\mathrm{b}}\dot{\eta}_r^{\mathrm{bs}}(t),$$

(2.68)

respectively, and the forward modal coupling term for the bimorph configuration is

$$\varphi_r^{\mathrm{b}} = -\frac{e_{31}b(h_{\mathrm{pb}} + h_{sb})}{2}\int_0^L \frac{\mathrm{d}^2\phi_r(x)}{\mathrm{d}x^2}\mathrm{d}x = -\frac{e_{31}(h_{\mathrm{pb}} + h_{sb})b}{2}\left.\frac{\mathrm{d}\phi_r(x)}{\mathrm{d}x}\right|_L.$$

(2.69)

Equations (2.64) and (2.67) are the coupled equations for the modal mechanical response $\eta_r^{\mathrm{bs}}(t)$ of the bimorph and the voltage response $v_{\mathrm{bs}}(t)$ across the resistive load. For harmonic base motions ($g(t) = Y_0\,\mathrm{e}^{\mathrm{j}\omega t}$ and $h(t) = \theta_0\,\mathrm{e}^{\mathrm{j}\omega t}$), the modal mechanical forcing $f_r(t)$ function becomes $f_r(t) = F_r\,\mathrm{e}^{\mathrm{j}\omega t}$, where F_r is given by Eq. (2.58).

The steady-state voltage response across the resistive load can then be obtained as

$$v_{\mathrm{bs}}(t) = \frac{\displaystyle\sum_{r=1}^{\infty}\frac{\mathrm{j}\omega\varphi_r^{\mathrm{b}}F_r}{\omega_r^2 - \omega^2 + \mathrm{j}2\zeta_r\omega_r\omega}}{\dfrac{1}{R_{\mathrm{l}}} + \mathrm{j}\omega\dfrac{C_{\mathrm{pb}}}{2} + \displaystyle\sum_{r=1}^{\infty}\frac{\mathrm{j}\omega\varphi_r^{\mathrm{b}}\chi_r^{\mathrm{bs}}}{\omega_r^2 - \omega^2 + \mathrm{j}2\zeta_r\omega_r\omega}}\mathrm{e}^{\mathrm{j}\omega t},$$

(2.70)

and the transverse displacement response of the bimorph relative to its base is

$$w_{\mathrm{rel}}^{\mathrm{bs}}(x, t) = \sum_{r=1}^{\infty}\left(F_r - \chi_r^{\mathrm{bs}}\frac{\displaystyle\sum_{r=1}^{\infty}\frac{\mathrm{j}\omega\varphi_r^{\mathrm{b}}F_r}{\omega_r^2 - \omega^2 + \mathrm{j}2\zeta_r\omega_r\omega}}{\dfrac{1}{R_{\mathrm{l}}} + \mathrm{j}\omega\dfrac{C_{\mathrm{pb}}}{2} + \displaystyle\sum_{r=1}^{\infty}\frac{\mathrm{j}\omega\varphi_r^{\mathrm{b}}\chi_r^{\mathrm{bs}}}{\omega_r^2 - \omega^2 + \mathrm{j}2\zeta_r\omega_r\omega}}\right)\frac{\phi_r(x)\mathrm{e}^{\mathrm{j}\omega t}}{\omega_r^2 - \omega^2 + \mathrm{j}2\zeta_r\omega_r\omega}.$$

(2.71)

2.3.4.2 Parallel Connection of the Piezoceramic Layers

The coupled equation of motion for the modal mechanical response can be obtained as

$$\ddot{\eta}_r^{\mathrm{bp}}(t) + 2\zeta_r\omega_r\dot{\eta}_r^{\mathrm{bp}}(t) + \omega_r{}^2\eta_r^{\mathrm{bp}}(t) + \chi_r^{\mathrm{bp}}v_{\mathrm{bp}}(t) = f_r(t), \tag{2.72}$$

where $\eta_r^{\mathrm{bp}}(t)$ is the modal mechanical response of the bimorph cantilever for parallel connection of the piezoceramic layers and $v_{\mathrm{bp}}(t)$ is the voltage across the resistive load (b stands for *bimorph configuration* and p stands for *parallel connection*). The modal mechanical forcing function $f_r(t)$ is given by Eq. (2.53) and the backward modal coupling term in Eq. (2.72) is

$$\chi_r^{\mathrm{bp}} = \vartheta_{\mathrm{bp}} \left.\frac{\mathrm{d}\phi_r(x)}{\mathrm{d}x}\right|_L, \tag{2.73}$$

where the coupling term in the physical coordinates can be given by

$$\vartheta_{\mathrm{bp}} = \frac{e_{31}b}{h_{\mathrm{pb}}}\left[\frac{h_{\mathrm{sb}}^2}{4} - \left(h_{\mathrm{pb}} + \frac{h_{\mathrm{sb}}}{2}\right)^2\right]. \tag{2.74}$$

Here, b is the width of the beam, h_{pb} and h_{sb} are the thicknesses of the piezoceramic and the substructure layers of the bimorph configuration displayed in Fig. 2.7c, respectively.

The electrical circuit equation for the parallel connection case is

$$C_{\mathrm{pb}}\dot{v}_{\mathrm{bp}}(t) + \frac{v_{\mathrm{bp}}(t)}{2R_{\mathrm{l}}} = i_{\mathrm{p}}^{\mathrm{bp}}(t), \tag{2.75}$$

where the internal capacitance and the current source terms are

$$C_{\mathrm{pb}} = \frac{\varepsilon_{33}^S bL}{h_{\mathrm{pb}}} \qquad i_{\mathrm{p}}^{\mathrm{bp}}(t) = \sum_{r=1}^{\infty} \varphi_r^{\mathrm{b}}\dot{\eta}_r^{\mathrm{bp}}(t), \tag{2.76}$$

respectively, and the forward modal coupling term φ_r^{b} is given by Eq. (2.69).

Equations (2.72) and (2.75) constitute the coupled equations for the modal mechanical response $\eta_r^{\mathrm{bp}}(t)$ of the bimorph and the voltage response $v_{\mathrm{bp}}(t)$ across the resistive load. For harmonic base motions, one can obtain the steady-state voltage response across the resistive load as

$$v_{\mathrm{bp}}(t) = \frac{\displaystyle\sum_{r=1}^{\infty}\frac{\mathrm{j}\omega\varphi_r^{\mathrm{b}}F_r}{\omega_r{}^2-\omega^2+\mathrm{j}2\zeta_r\omega_r\omega}}{\frac{1}{2R_{\mathrm{l}}} + \mathrm{j}\omega C_{\mathrm{pb}} + \displaystyle\sum_{r=1}^{\infty}\frac{\mathrm{j}\omega\varphi_r^{\mathrm{b}}\chi_r^{\mathrm{bp}}}{\omega_r{}^2-\omega^2+\mathrm{j}2\zeta_r\omega_r\omega}}\mathrm{e}^{\mathrm{j}\omega t}, \tag{2.77}$$

and the transverse displacement response of the bimorph relative to its base can be expressed as

$$
w_{\text{rel}}^{\text{bp}}(x, t) = \sum_{r=1}^{\infty} \left(F_r - \chi_r^{\text{bp}} \frac{\sum_{r=1}^{\infty} \frac{j\omega\varphi_r^{\text{b}} F_r}{\omega_r^2 - \omega^2 + j2\zeta_r\omega_r\omega}}{\frac{1}{2R_l} + j\omega C_{\text{pb}} + \sum_{r=1}^{\infty} \frac{j\omega\varphi_r^{\text{b}} \chi_r^{\text{bp}}}{\omega_r^2 - \omega^2 + j2\zeta_r\omega_r\omega}} \right) \frac{\phi_r(x)e^{j\omega t}}{\omega_r^2 - \omega^2 + j2\zeta_r\omega_r\omega}.
$$

$$(2.78)$$

2.3.5 Single-Mode Electromechanical Equations

The steady-state voltage response and vibration response expressions obtained in Sections 2.3.3 and 2.3.4 are valid for harmonic excitations at any arbitrary frequency ω. That is, these expressions are the *multi-mode* solutions as they include all vibration modes of the respective cantilevered piezoelectric energy harvester beams. Hence, the resulting equations can predict the coupled systems dynamics not only for resonance excitations but also for excitations at the off-resonance frequencies of the configurations shown in Fig. 2.7.

Resonance excitation is a special case of the derivation given here and is commonly used in the literature in order to investigate the maximum performance of the harvester in electrical power generation. Therefore, excitation of a unimorph/bimorph at or very close to one of its natural frequencies is a very useful problem to investigate through the resulting equations derived in Sections 2.3.3 and 2.3.4. This is the *modal excitation* condition and mathematically it corresponds to $\omega \cong \omega_r$. With this assumption on the excitation frequency, the major contribution in the summation terms of Eqs. (2.61), (2.63), (2.70), (2.71), (2.77) and (2.78) are from the rth vibration mode, which allows drastic simplifications in the coupled voltage response and vibration response expressions. In the following, the reduced *single-mode* expressions are given for excitations at or very close to the r-th natural frequency. However, it should be noted that the fundamental vibration mode is the main concern in the energy harvesting problem (which corresponds to $r = 1$).

2.3.5.1 Unimorph Configuration

If the unimorph configuration shown in Fig. 2.7a is excited at $\omega \cong \omega_r$, the contribution of all the vibration modes other than the rth mode can be ignored in the summation terms. Then, the steady-state voltage response given by Eq. (2.61) can be reduced to

$$
\hat{v}_{\text{u}}(t) = \frac{j\omega R_l \varphi_r^{\text{u}} F_r \, e^{j\omega t}}{(1 + j\omega R_l C_{\text{pu}})(\omega_r^2 - \omega^2 + j2\zeta_r\omega_r\omega) + j\omega R_l \varphi_r^{\text{u}} \chi_r^{\text{u}}},
$$

$$(2.79)$$

and the transverse displacement relative to the moving base is obtained from equation Eq. (2.63) as

$$\hat{w}_{\text{rel}}^{\text{u}}(x, t) = \frac{\left(1 + j\omega R_1 C_{\text{pu}}\right) F_r \phi_r(x) e^{j\omega t}}{(1 + j\omega R_1 C_{\text{pu}})(\omega_r{}^2 - \omega^2 + j2\zeta_r \omega_r \omega) + j\omega R_1 \varphi_r^{\text{u}} \chi_r^{\text{u}}}. \tag{2.80}$$

Here and below, a hat (^) denotes that the respective term is reduced from the full (multi-mode) solution for excitations very close to a natural frequency. The relevant terms in Eqs. (2.79) and (2.80) can be found in Section 2.3.3.

2.3.5.2 Bimorph Configuration (Series Connection)

For excitation of the bimorph shown in Fig. 2.7b around its rth natural frequency, the single-mode steady-state voltage response given by Eq. (2.70) can be reduced to

$$\hat{v}_{\text{bs}}(t) = \frac{j2\omega R_1 \varphi_r^{\text{b}} F_r \, e^{j\omega t}}{(2 + j\omega R_1 C_{\text{pb}})(\omega_r{}^2 - \omega^2 + j2\zeta_r \omega_r \omega) + j2\omega R_l \varphi_r^{\text{b}} \chi_r^{\text{bs}}}. \tag{2.81}$$

Similarly, the transverse displacement relative to the moving base is reduced from Eq. (2.71) as

$$\hat{w}_{\text{rel}}^{\text{bs}}(x, t) = \frac{(2 + j\omega R_1 C_{\text{pb}}) F_r \phi_r(x) e^{j\omega t}}{(2 + j\omega R_1 C_{\text{pb}})(\omega_r{}^2 - \omega^2 + j2\zeta_r \omega_r \omega) + j2\omega R_1 \varphi_r^{\text{b}} \chi_r^{\text{bs}}}, \tag{2.82}$$

where the relevant terms can be found in Section 2.3.4.1.

2.3.5.3 Bimorph Configuration (Parallel Connection)

If the bimorph configuration displayed in Fig. 2.7c is excited at $\omega \cong \omega_r$, the steady-state voltage response given by Eq. (2.77) can be reduced to

$$\hat{v}_{\text{bp}}(t) = \frac{j2\omega R_1 \varphi_r^{\text{b}} F_r \, e^{j\omega t}}{(1 + j2\omega R_1 C_{\text{pb}})(\omega_r{}^2 - \omega^2 + j2\zeta_r \omega_r \omega) + j2\omega R_l \varphi_r^{\text{b}} \chi_r^{\text{bp}}}, \tag{2.83}$$

and the transverse displacement relative to the base is obtained from Eq. (2.78) as

$$\hat{w}_{\text{rel}}^{\text{bp}}(x, t) = \frac{(1 + j2\omega R_1 C_{\text{pb}}) F_r \phi_r(x) e^{j\omega t}}{(1 + j2\omega R_1 C_{\text{pb}})(\omega_r{}^2 - \omega^2 + j2\zeta_r \omega_r \omega) + j2\omega R_1 \varphi_r^{\text{b}} \chi_r^{\text{bp}}}, \tag{2.84}$$
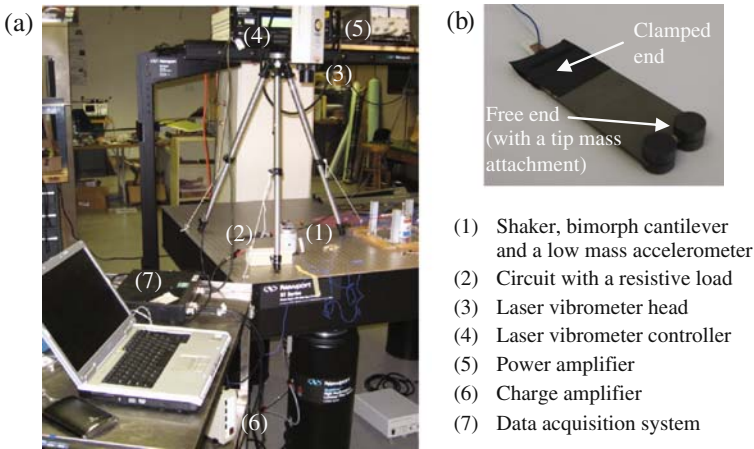
where the relevant terms can be found in Section 2.3.4.2.

2.3.6 Experimental Validation

The aim of this section is to validate the distributed parameter relations for a bimorph cantilever with a tip mass experimentally. The experimentally measured voltage response-to-base acceleration FRFs and the vibration response-to-base acceleration FRFs are compared with the closed-form relations derived in this chapter. Variations of the voltage output and the tip velocity response of the bimorph with changing load resistance are also investigated and predicted using the analytical relations. Optimum resistive loads of the bimorph cantilever are identified for excitations at the short-circuit and open-circuit resonance frequencies.

2.3.6.1 Experimental Setup

The experimental setup used for measuring the voltage-to-base acceleration and tip velocity-to-base acceleration FRFs of the bimorph cantilever is shown in Fig. 2.8a. The bimorph cantilever analyzed in this experiment is displayed in Fig. 2.8b and is manufactured by Piezo Systems, Inc. (T226-A4-503X). The same type of bimorph was used by duToit et al. (2007) for verification of their Rayleigh–Ritz type of approximate model. In that work, duToit et al. (2007) underestimated the vibration response and the power outputs especially around the resonance frequency and they attributed this inaccuracy in the results to the "unmodeled nonlinear piezoelectric response."

Here, a tip mass is attached to the bender to make the problem relatively sophisticated in terms of modeling (Fig. 2.8b). The bimorph consists of two oppositely poled PZT-5A piezoceramic layers bracketing a brass substructure layer. Therefore, the piezoelectric elements are connected in series as given in Fig. 2.7b. Table 2.1 shows


(a)

(b) Clamped end

Free end (with a tip mass attachment)

(1) Shaker, bimorph cantilever and a low mass accelerometer
(2) Circuit with a resistive load
(3) Laser vibrometer head
(4) Laser vibrometer controller
(5) Power amplifier
(6) Charge amplifier
(7) Data acquisition system

Fig. 2.8 (**a**) Experimental setup and the equipments used for analyzing the bimorph cantilever and (**b**) a detailed view of the bimorph cantilever with a tip mass

Table 2.1 Geometric and material parameters of the bimorph cantilever used for the experimental validation

Geometric Parameters	Piezoceramic		Substructure
Length, L (mm)	50.8		50.8
Width, b (mm)	31.8		31.8
Thickness, h (mm)	0.26 (each)		0.14
Tip mass, M_t (kg)		0.012	
Material Parameters	**Piezoceramic (PZT-5A)**		**Substructure (Brass)**
Mass density, ρ (kg/m^3)	7800		9000
Young's modulus, Y (GPa)	66		105
Piezo. constant, d_{31} (pm/V)	-190		–
Permittivity, ε_{33}^S (nF/m)	$1500\varepsilon_0$		–

the geometric and material properties of the piezoceramic and the substructure layers, respectively. Note that the length described by L is the overhang length of the harvester in the clamped condition, i.e., it is not the total free length (63.5 mm) of the bender as acquired from the manufacturer. In addition, permittivity component at constant strain is given in Table 2.1 in terms of the permittivity of free space, $\varepsilon_0 = 8.854$ pF/m (IEEE, 1987).

The bimorph cantilever shown in Fig. 2.8b is excited from its base with a sine sweep generated by an electromagnetic LDS shaker. The base acceleration of the harvester is measured by a low mass accelerometer (PCB U352C22) on the shaker and the velocity response of the harvester at the free end is measured by a laser vibrometer (Polytec OFV303 laser sensor head, OFV3001 controller). The experimental voltage FRF (in V/g) and tip velocity FRF (in (m/s)/g) obtained for a resistive load of 1 kΩ are shown in Fig. 2.9a (where g is the gravitational acceleration). The coherence functions of these measurements are given by Fig. 2.9b. The coherence is considerably low for frequencies less than 30 Hz but it is good around the first resonance frequency (which is approximately 45.6 Hz for a 1 kΩ resistive load).
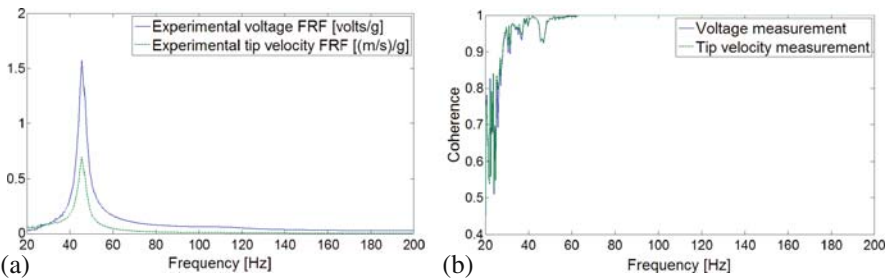
Fig. 2.9 (**a**) Experimental voltage and tip velocity FRFs of the bimorph cantilever and (**b**) their coherence functions (for a resistive load of 1 kΩ)

2.3.6.2 Validation of the Distributed Parameter Model

Since the vibration mode seen around $45.6\,\text{Hz}$ (for $1\,\text{k}\Omega$) is the only mode in a wide frequency range and as this is the mode of primary concern (i.e., the most flexible vibration mode), the single-mode relations given by Eqs. (2.81) and (2.82) are used for predicting the electromechanical FRFs. Note that the base of the cantilever is not rotating, i.e., $\theta_0 = 0$ in Eq. (2.58). In addition, Eq. (2.82) must be rearranged in order to predict the experimental velocity measurement since the laser vibrometer measures the *absolute* velocity response at the tip of the beam (rather than the velocity *relative* to the moving base). Thus, the electromechanical FRFs used for predicting the experimental measurements can be extracted from Eqs. (2.81) and (2.82) as

$$
\frac{\hat{v}_{\text{bs}}(t)}{-\omega^2 Y_0\, \text{e}^{\text{j}\omega t}} = \frac{-\text{j}2\omega R_l \varphi_r^{\text{b}}\left(m \int\limits_0^L \phi_r(x)\text{d}x + M_t \phi_r(L) \right)}{(2 + \text{j}\omega R_l C_{\text{pb}})(\omega_r{}^2 - \omega^2 + \text{j}2\zeta_r \omega_r \omega) + \text{j}2\omega R_l \varphi_r^{\text{b}} \chi_r^{\text{bs}}},
\tag{2.85}
$$

$$
\frac{\frac{\text{d}\hat{w}^{\text{bs}}(L,t)}{\text{d}t}}{-\omega^2 Y_0\, \text{e}^{\text{j}\omega t}} = \frac{1}{\text{j}\omega} + \frac{-\text{j}\omega(2 + \text{j}\omega R_l C_{\text{pb}})\left(m \int\limits_0^L \phi_r(x)\text{d}x + M_t \phi_r(L) \right)\phi_r(L)}{(2 + \text{j}\omega R_l C_{\text{pb}})(\omega_r{}^2 - \omega^2 + \text{j}2\zeta_r \omega_r \omega) + \text{j}2\omega R_l \varphi_r^{\text{b}} \chi_r^{\text{bs}}},
\tag{2.86}
$$

where $r = 1$ since the vibration mode of interest is the fundamental vibration mode.

In order to identify the modal mechanical damping ratio, one way is to force the system to short-circuit conditions (by shorting the electrodes of the bimorph) as done by duToit et al. (2007). However, if the electromechanical model is *self-consistent*, one must be able to identify the mechanical damping ratio for any value of load resistance. Furthermore, either the voltage FRF or the tip velocity FRF can be used for identifying modal mechanical damping ratio, since the bimorph energy harvester itself is a *transducer*. In other words, theoretically, the coupled tip velocity information is included in the voltage output information of the harvester, and the voltage and tip motion predictions for the same mechanical damping ratio must be in agreement.

The mechanical damping ratio of the first vibration mode is identified as $\zeta_1 = 0.027$ using the voltage FRF as shown in Fig. 2.10a (for $1\,\text{k}\Omega$ load resistance). For this identified damping ratio, the voltage FRF of the model (obtained from Eq. (2.85)) is in perfect agreement with the experimental FRF as shown in Fig. 2.10a. As discussed in the previous paragraph, for the same damping ratio (2.7%), the tip velocity FRF obtained from the model should predict the experimental tip velocity FRF accurately. The tip velocity FRF obtained from Eq. (2.86) for 2.7% mechanical damping is plotted with the laser vibrometer measurement in Fig. 2.10b. The agreement between the theoretical and the experimental tip velocity FRFs is very good, which clearly shows the consistency of the linear electromechanical model proposed here.
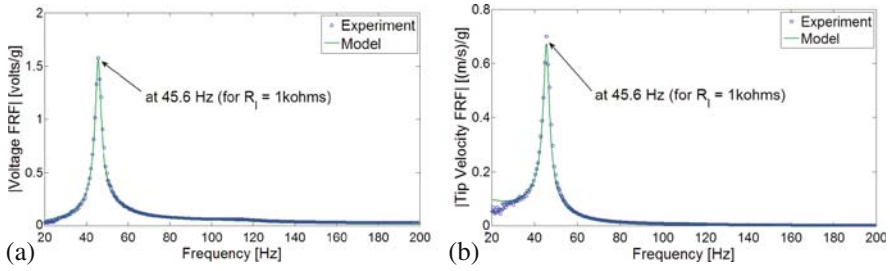
Fig. 2.10 Comparison of the model predictions and the experimental measurements; (**a**) voltage FRF and (**b**) tip velocity FRF (for 1 kΩ)

The experimental measurements are repeated for eight different values of load resistance: 1, 6.7, 11.8, 22, 33, 47, 100, and 470 kΩ. Each of the resistive loads results in a different voltage FRF and a tip velocity FRF. Figure 2.11a and 2.11b, respectively, display enlarged views of the voltage output and tip velocity FRFs around the first vibration mode for these eight different values of load resistance. The direction of increasing load resistance is depicted with an arrow and it is clear from Fig. 2.11a that the voltage across the resistive load increases monotonically with increasing load resistance at every excitation frequency. For the extreme values of the load resistance, the frequency of maximum voltage output moves from the short-circuit resonance frequency (for $R_\mathrm{l} \rightarrow 0$) to the open-circuit resonance frequency (for $R_\mathrm{l} \rightarrow \infty$). The experimentally obtained short-circuit and open-circuit resonance frequencies for the first mode of this cantilever are approximately 45.6 and 48.4 Hz, respectively. The analytical model predicts these two frequencies as 45.7 and 48.2 Hz, respectively. For a moderate value of load resistance, the frequency of maximum voltage has a value in between these two extreme frequencies. Even for more sophisticated energy harvesting circuits, the resonance frequency of the beam usually takes a value between these two extreme frequencies since the impedance across the electrodes can change at most from zero to infinity regardless of the circuit elements. This can be observed in the experimental vibration FRF (Lesieutre et al., 2004) of a cantilevered piezoelectric energy harvester beam con-
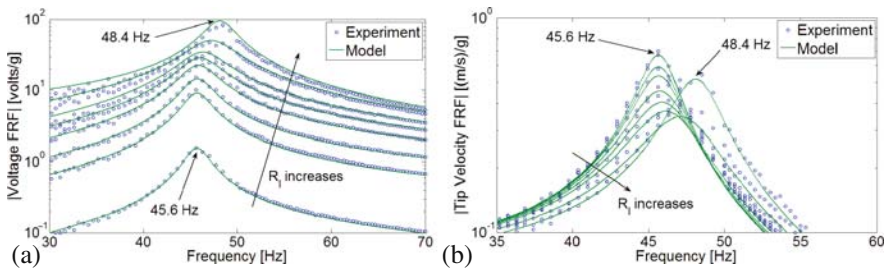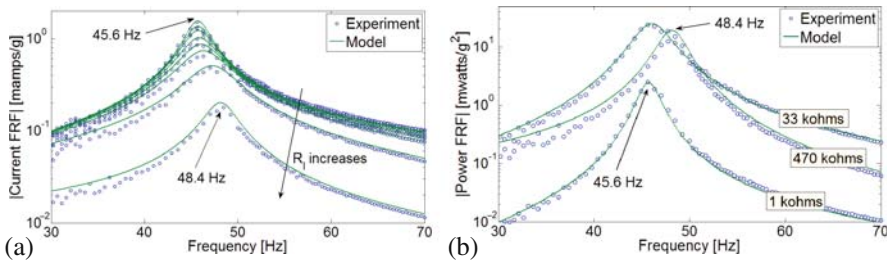

Fig. 2.11 Enlarged views of the (**a**) voltage FRFs and the (**b**) tip velocity FRFs for eight different values of load resistance (model predictions and the experimental measurements)

nected to an electrical circuit with more complicated elements (such as a full-wave rectifier).

The shift in the frequencies of the maximum response amplitude is also the case in the tip velocity FRF (Fig. 2.11b). However, the variation of tip velocity with load resistance is not necessarily monotonic at every frequency. For excitation at 45.6 Hz, the tip motion is suppressed as the resistive load is increased up to a certain value. It is very important to note that this suppression in the motion amplitude is more sophisticated than viscous damping. With increasing load resistance (up to a certain value), the motion is *attenuated* at 45.6 Hz, whereas it is *amplified* at 48.4 Hz. Hence, if one focuses on the open-circuit resonance frequency (48.4 Hz), *both the voltage output and the vibration amplitude* at the tip of the beam *increase* with increasing load resistance. Therefore, modeling the effect of piezoelectric coupling in the beam equation as viscous damping clearly *fails* in predicting this phenomenon (as it cannot predict the frequency shift due to changing load resistance). Note that, for eight different resistive loads, the model successfully predicts the frequency response of the voltage output and tip velocity (where the mechanical damping ratio is kept constant at 2.7%).

The electric current FRF (obtained from $I = V/R_l$) exhibits the opposite behavior of the voltage FRF with changing load resistance as shown in Fig. 2.12a. Hence, the electric current decreases monotonically with increasing load resistance at every excitation frequency. Figure 2.12b displays the electrical power FRF for three different resistive loads.[5] The trend in the electrical power FRF with changing load resistance is more interesting as it is the multiplication of two FRFs (voltage and current) with the opposite trends. As can be seen in Fig. 2.12b, the electrical power FRFs for different resistive loads intersect each other just like the tip velocity FRFs (Fig. 2.11b). For a given excitation frequency, there exists a certain value of load resistance that gives the maximum electrical power. This value is called the *optimum*


Fig. 2.12 Enlarged views of the (**a**) current FRFs for eight different values of load resistance and the (**b**) power FRFs for three different values of load resistance (model predictions and experimental measurements)

---

[5] In order to avoid confusion with 8 intersecting curves, the electrical power FRFs are given for 3 resistive loads only.

load resistance and can be observed more easily if the frequency of interest is kept constant and the power amplitude is plotted against load resistance as addressed next.[6]

The short-circuit and open-circuit resonance frequencies of the first mode are defined for the extreme cases of load resistance (45.6 Hz as $R_1 \rightarrow 0$ and 48.4 Hz as $R_1 \rightarrow \infty$) and these frequencies are of practical interest. The variation of the voltage output with changing load resistance for excitations at these two frequencies are shown in Fig. 2.13a. In both cases, voltage increases monotonically with load resistance. The voltage output for excitation at the short-circuit resonance frequency is larger when the system is close to short-circuit conditions and vice versa. The maximum voltage amplitude in the limit $R_1 \rightarrow \infty$ is about 54.5 V/g for excitation at 45.6 Hz and is about 108.8 V/g for excitation at 48.4 Hz. Figure 2.13b displays the variation of the electric current with changing load resistance for excitations at these two frequencies. The trend of the current amplitude with changing load resistance is opposite to that of the voltage amplitude. That is, the current amplitude decreases monotonically with increasing load resistance. The current output for excitation at the short-circuit resonance frequency is larger when the system is close to short-circuit conditions and vice versa. In the limit $R_1 \rightarrow 0$, the maximum current
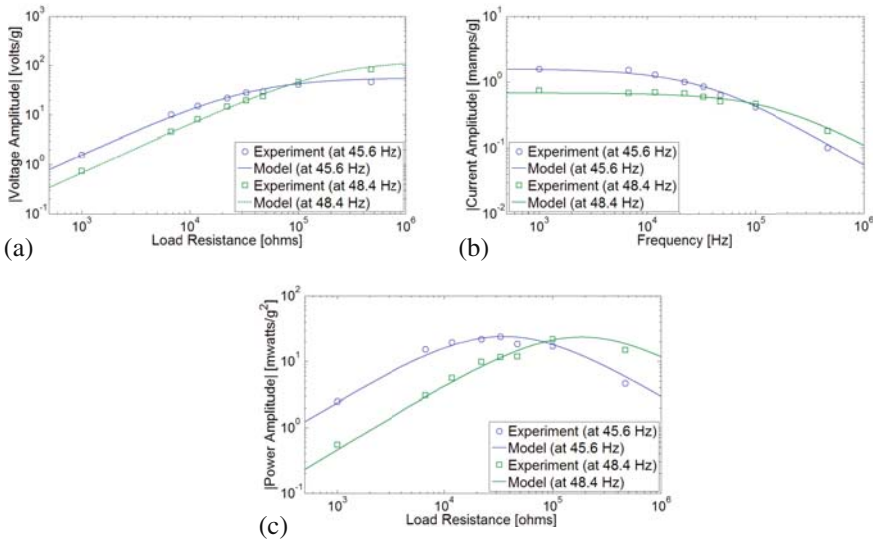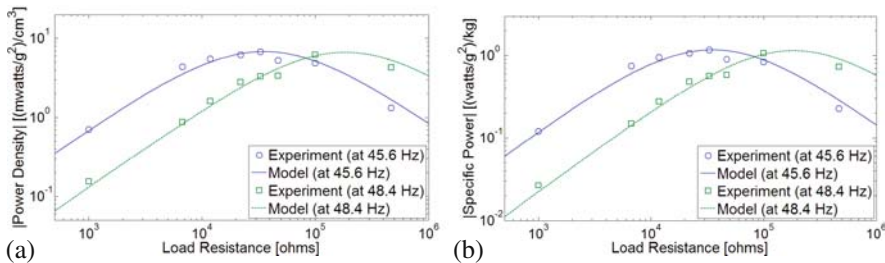

Fig. 2.13 Variations of the (**a**) voltage amplitude, (**b**) current amplitude, and the (**c**) electrical power amplitude with load resistance for excitations at the short-circuit and open-circuit resonance frequencies of the first vibration mode

---

[6] The amplitudes given in the voltage, current and tip velocity FRFs are the peak amplitudes (not the root mean square values). Therefore, the electrical power amplitude is the peak power amplitude (which is twice the average power).

amplitude is about $1.57\,mA/g$ for excitation at $45.6\,Hz$ and is about $0.68\,mA/g$ for excitation at $48.4\,Hz$.

The variation of the electrical power with changing load resistance is given in Fig. 2.13c for the short-circuit and open-circuit resonance frequency excitations. These two excitation frequencies have different optimum resistive loads which yield the maximum electrical power. The optimum load resistance for excitation at $45.6\,Hz$ is about $35\,k\Omega$, yielding a maximum electrical power of about $23.9\,mW/g^2$, whereas the optimum resistive load for excitation at $48.4\,Hz$ is $186\,k\Omega$, yielding approximately the same power output. As in the case of the voltage and current outputs, the electrical power output for excitation at the short-circuit resonance frequency is larger when the system is close to short-circuit conditions and vice versa. The respective trends in the electrical outputs at the short-circuit and open-circuit resonance frequencies of the first mode are successfully predicted by the single-mode analytical relations derived in this chapter.

A useful practice to obtain some additional information regarding the performance of the energy harvester device results from dividing the electrical power by the volume and by the mass of the device. The total overhang volume of the device (including the volume of the tip mass) is about $3.52\,cm^3$ and the total overhang mass of the device is about $20.6\,g$. The electrical power versus load resistance graph given by Fig. 2.13c can therefore be used to obtain the maximum *power density* (power per device volume) and *specific power* (power per device mass) values. The variations of the power density and the specific power with load resistance are given by Fig. 2.14a and 2.14b, respectively (for the short-circuit and open-circuit resonance excitations). For instance, for excitation at $45.6\,Hz$, the maximum power density is about $6.8\,(mW/g^2)/cm^3$ and the maximum specific power is about $1.15\,(W/g^2)/kg$ (for a $35\,k\Omega$ resistive load). It is very important to note that the power density and the specific power concepts are *not* complete non-dimensional representations. For instance, the same device volume can be occupied by the same amount of material (piezoceramic, substructure, and tip mass) for a different aspect ratio of the beam, yielding a larger or smaller electrical power with totally different natural frequencies. However, these representations have been found useful for comparison of the energy harvester devices in the literature.

Fig. 2.14 Variations of the (**a**) power density and the (**b**) specific power amplitudes with load resistance for excitations at the short-circuit and open-circuit resonance frequencies of the first vibration mode

References

Ajitsaria J, Choe S Y, Shen D, and Kim D J 2007 Modeling and analysis of a bimorph piezoelectric cantilever beam for voltage generation *Smart Materials and Structures* **16**:447–454

Anton S R and Sodano H A 2007 A review of power harvesting using piezoelectric materials (2003–2006) *Smart Materials and Structures* **16**:R1–R21

Arnold D 2007 Review of microscale magnetic power generation *IEEE Transactions on Magnetics* **43**:3940–3951

Banks T L and Inman D J 1991 On damping mechanisms in beams *ASME Journal of Applied Mechanics* **58**:716–723

Beeby S P, Tudor M J, and White N M 2006 Energy harvesting vibration sources for microsystems applications, *Measurement Science and Technology* **13**:175–195

Chen S -N, Wang G –J, and Chien M -C 2006 Analytical modeling of piezoelectric vibration-induced micro power generator, *Mechatronics* **16**:387–397

Clough R W and Penzien J 1975 *Dynamics of Structures* John Wiley and Sons, New York

Cook-Chennault K A, Thambi N, and Sastry A M 2008 Powering MEMS portable devices – a review of non-regenerative and regenerative power supply systems with emphasis on piezo-electric energy harvesting systems, *Smart Materials and Structures* **17**:043001:1–33

Crandall S H, Karnopp D C, Kurtz Jr E F, and Pridmore-Brown D C 1968 *Dynamics of Mechanical and Electromechanical Systems* McGraw-Hill, New York

Daqaq M, Renno J M, Farmer J R, and Inman D J 2007 Effects of system parameters and damping on an optimal vibration-based energy harvester *Proceedings of the 48th AIAA/ASME/ASCE/AHS/ASC Structures, Structural Dynamics, and Materials Conference*

duToit N E, Wardle B L, and Kim S-G 2005 Design considerations for MEMS-scale piezoelectric mechanical vibration energy harvesters, *Integrated Ferroelectrics* **71**:121–160

duToit N E and Wardle B L 2007 Experimental verification of models for microfabricated piezo-electric vibration energy harvesters, *AIAA Journal* **45**:1126–1137

Elvin N and Elvin A 2008 A general equivalent circuit model for piezoelectric generators, *Journal of Intelligent Material Systems and Structures* **19** in press (DOI: 10.1177/1045389X08089957)

Erturk A and Inman D J 2008a On mechanical modeling of cantilevered piezoelectric vibration energy harvesters, *Journal of Intelligent Material Systems and Structures* **19**:1311–1325

Erturk A and Inman D J 2008b Issues in mathematical modeling of piezoelectric energy harvesters, *Smart Materials and Structures* in press

Erturk A and Inman D J 2008c A distributed parameter electromechanical model for cantilevered piezoelectric energy harvesters, *ASME Journal of Vibration and Acoustics* **130**:041002-1-15

Erturk A and Inman D J 2008d An experimentally validated bimorph cantilever model for piezo-electric energy harvesting from base excitations, *Smart Materials and Structures* accepted

Erturk A and Tarazaga P A, Farmer J R, and Inman D J 2008e Effect of strain nodes and electrode configuration on piezoelectric energy harvesting from cantilevered beams, *ASME Journal of Vibration and Acoustics* in press (DOI: 10.1115/1.2981094)

Fang H-B, Liu J-Q, Xu Z-Y, Dong L, Chen D, Cai B-C, and Liu Y 2006 A MEMS-based piezo-electric power generator for low frequency vibration energy harvesting, *Chinese Physics Letters* **23**:732–734

Glynne-Jones P, Tudor M J, Beeby S P, and White N M 2004 An electromagnetic, vibration-powered generator for intelligent sensor systems, *Sensors and Actuators A* **110**:344–349

Hagood N W, Chung W H, and Von Flotow A 1990 Modelling of piezoelectric actuator dynamics for active structural control, *Journal of Intelligent Material Systems and Structures* **1**:327–354

IEEE Standard on Piezoelectricity 1987 IEEE, New York.

Jeon Y B, Sood R, Jeong J H, and Kim S 2005 MEMS power generator with transverse mode thin film PZT, *Sensors & Actuators A* **122**:16–22

Lesieutre G A, Ottman G K, and Hofmann H F 2004 Damping as a result of piezoelectric energy harvesting, *Journal of Sound and Vibration* **269**:991–1001

Lin J H, Wu X M, Ren T L, and Liu L T 2007 Modeling and simulation of piezoelectric MEMS energy harvesting device, *Integrated Ferroelectrics* **95**:128–141.

Lu F, Lee H, and Lim S 2004 Modeling and analysis of micro piezoelectric power generators for micro-electromechanical-systems applications, *Smart Materials and Structures* **13**:57–63

Mitcheson P, Miao P, Start B, Yeatman E, Holmes A, and Green T 2004 MEMS electrostatic micro-power generator for low frequency operation, *Sensors and Actuators A* **115**:523–529

Ottman G K, Hofmann H F, Bhatt A C, and Lesieutre G A 2002 Adaptive piezoelectric energy harvesting circuit for wireless remote power supply, *IEEE Transactions on Power Electronics* **17**:669–676.

Priya S 2007 Advances in energy harvesting using low profile piezoelectric transducers, *Journal of Electroceramics* **19**:167–184

Roundy S, Wright P K, and Rabaey J 2002 Micro-electrostatic vibration-to-electricity converters *Proceedings of the ASME 2002 International Mechanical Engineering Congress and Exposition*

Roundy S, Wright P K, and Rabaey J 2003 A study of low level vibrations as a power source for wireless sensor nodes, *Computer Communications* **26**:1131–1144

Sodano H A, Inman D J, and Park G 2004a A review of power harvesting from vibration using piezoelectric materials, *The Shock and Vibration Digest* **36**:197–205

Sodano H A, Park G, and Inman D J 2004b Estimation of electric charge output for piezoelectric energy harvesting, *Strain* **40**:49–58

Sodano H, Inman D, and Park G 2005 Generation and storage of electricity from power harvesting devices, *Journal of Intelligent Material Systems and Structures* **16**:67–75

Stephen N G 2006 On energy harvesting from ambient vibration, *Journal of Sound and Vibration* **293**:409–425

Strutt J W (Lord Rayleigh) 1894 *The Theory of Sound* MacMillan Company, London

Timoshenko S, Young D H, and Weaver W 1974 *Vibration Problems in Engineering* John Wiley and Sons, New York

Williams C B and Yates R B 1996 Analysis of a micro-electric generator for microsystems, *Sensors and Actuators A* **52**:8–11